NeuroImage 297 (2024) 120747

Contents lists available at ScienceDirect

NeuroImage

journal homepage: www.elsevier.com/locate/ynimg

The connectivity-based architecture of the human piriform cortex

F. Zahnert [a,1,*], U. Kleinholdermann [b,c,1], M. Belke [a,d], B. Keil [e,f,g], K. Menzler [a,g], D.J. Pedrosa [b], L. Timmermann [b,g], T. Kircher [c,g], I. Nenadić [c,g], S. Knake [a,d,g,h]

[a] Epilepsy Center Hesse, Department of Neurology, University Hospital Marburg, Philipps-University Marburg, Germany
[b] Department of Neurology, University Hospital Marburg, Philipps University Marburg, Germany
[c] Department of Psychiatry and Psychotherapy, University Hospital Marburg, Philipps University Marburg, Germany
[d] Center for Personalized Translational Epilepsy Research, Goethe University Frankfurt, Germany
[e] Institute of Medical Physics and Radiation Protection, Mittelhessen University of Applied Sciences, Giessen, Germany
[f] Department of Diagnostic and Interventional Radiology, University Hospital Marburg, Philipps University of Marburg, Marburg, Germany
[g] Center for Mind, Brain and Behavior, Philipps University Marburg, Germany
[h] Core Facility Brain Imaging, Philipps University Marburg, Germany

ARTICLE INFO

Keywords:
Piriform cortex
Connectivity
Parcellation
Subregions
Diffusion MRI, fMRI

ABSTRACT

The anatomy of the human piriform cortex (PC) is poorly understood. We used a bimodal connectivity-based-parcellation approach to investigate subregions of the PC and its connectional differentiation from the amygdala.

One hundred (55 % female) genetically unrelated subjects from the Human Connectome Project were included. A region of interest (ROI) was delineated bilaterally covering PC and amygdala, and functional and structural connectivity of this ROI with the whole gray matter was computed. Spectral clustering was performed to obtain bilateral parcellations at granularities of $k = 2$–10 clusters and combined bimodal parcellations were computed. Validity of parcellations was assessed via their mean individual-to-group similarity per adjusted rand index (ARI).

Individual-to-group similarity was higher than chance in both modalities and in all clustering solutions. The amygdala was clearly distinguished from PC in structural parcellations, and olfactory amygdala was connectionally more similar to amygdala than to PC. At higher granularities, an anterior and ventrotemporal and a posterior frontal cluster emerged within PC, as well as an additional temporal cluster at their boundary. Functional parcellations also showed a frontal piriform cluster, and similar temporal clusters were observed with less consistency. Results from bimodal parcellations were similar to the structural parcellations. Consistent results were obtained in a validation cohort.

Distinction of the human PC from the amygdala, including its olfactory subregions, is possible based on its structural connectivity alone. The canonical fronto-temporal boundary within PC was reproduced in both modalities and with consistency. All obtained parcellations are freely available.

1. Introduction

The piriform cortex (PC) is a region of three-layered primary olfactory cortex at the mesial junction of the frontal and temporal lobes (Vaughan and Jackson, 2014). Evidence from animal studies suggests direct and extensive afferent connections from the olfactory bulb (Ghosh et al., 2011; Miyamichi et al., 2011) and projections to a variety of cortical and subcortical regions, including limbic and other olfactory regions (Johnson et al., 2000; Kajiwara et al., 2007; Krettek and Price, 1977). While the piriform cortex has been extensively studied in animal studies, there is much less evidence about its organization into subregions and their precise boundaries in humans (Zelano and Sobel, 2005). Besides, histological descriptions of the human cortex also lack granularity in this region (Brodman, 1909; von Economo and Koskinas, 1925).

Neuroimaging studies investigating the human piriform cortex and the adjacent olfactory system have generally referred to two histological descriptions (Allison, 1954; Mai et al., 2015, see also Echevarria-Cooper et al., 2022; Gottfried et al., 2002; Porter et al., 2005; Zhou et al., 2021, 2019). Here, it has been suggested that the PC consists of a frontal (f-PC)

* Corresponding author at: Abteilung für Neurologie, Baldingerstraße, 35043 Marburg, Germany.
E-mail address: zahnert@med.uni-marburg.de (F. Zahnert).
[1] equal contribution.

https://doi.org/10.1016/j.neuroimage.2024.120747
Received 28 December 2023; Received in revised form 16 July 2024; Accepted 18 July 2024
Available online 20 July 2024

and a temporal (t-PC) subdivision. Nonetheless, an exact boundary between these regions or even the boundaries of PC with adjacent cortex have not been delineated in detail. Functional neuroimaging rendered evidence for functional differences between f-PC and t-PC using manually defined ROIs. Here, the f-PC showed responses modulated by attention and hedonic tone (Bensafi et al., 2007; Gottfried et al., 2002; Zelano et al., 2005), whereas spatial information, i.e., which nostril is stimulated by an odor, seemed to be encoded in the t-PC (Porter et al., 2005). In addition, some authors postulate the existence of a "piriform-cortical amygdala area" (Borger et al., 2021; Galovic et al., 2019; Gonçalves Pereira et al., 2005) encompassing both the PC and the olfactory amygdala (consisting of cortical amygdala, periamygdaloid complex and medial amygdala (Allison, 1954)).

The abovementioned neuroimaging studies of the piriform cortex largely relied on its manual delineation on T1-images (Zelano et al., 2005; Bensafi et al., 2007; Borger et al., 2021; Galovic et al., 2019; Gonçalves Pereira et al., 2005), which can lead to bias and mislabeling, as the boundaries of the PC are not visible on structural MRI scans. One approach to overcome this has been an automated segmentation of the PC, which, however, relied on a manual definition of the PC and, too, used structural imaging data as input (Steinbart et al., 2023). Therefore, a data-driven approach for the delineation of the PC without prior assumptions concerning its boundaries could be beneficial for future neuroimaging studies of the piriform cortex.

Recently, clustering of subregions within the olfactory system based on resting state functional connectivity has been reported (Zhou et al., 2019). Within the PC, these authors bilaterally demonstrated a subdivision into t-PC and f-PC. However, in this important study, the adjacent periamygdaloid cortex (PAC) and amygdala were excluded from clustering. Therefore, the mesial boundaries of the t-PC and the differentiation of the PC from surrounding gray matter structures based on in vivo neuroimaging remain to be clarified.

The aims of the present study were twofold. First, we aimed to investigate the boundaries of the PC within a large ROI including surrounding gray matter in vivo. Parcellation based on structural and functional connectivity was assessed, allowing analysis not only of the temporomesial extent of clusters within the PC but also of the relationship of the PC to the olfactory amygdala. Second, we examined subregional parcellations of the PC based on both modalities and investigated whether previously reported subdivisions into t-PC and f-PC could be validated within this large ROI. To aid future neuroimaging studies of the human olfactory system we make the resulting data-driven parcellations of the piriform cortex freely available.

2. Methods

2.1. Subjects

One hundred randomly drawn unrelated subjects from the S1200 release of the Human Connectome Project (HCP) in whom an ICA-processed rs-fMRI scan, diffusion MRI and structural MRI were available were included (Van Essen et al., 2012; Sotiropoulos et al., 2013). Subjects were healthy adults (55 % female) aged 22 to 35 years. A validation cohort of 100 further unrelated subjects (47 female) from the same dataset who were also unrelated to the subjects of the first dataset was analyzed to assess reproducibility of parcellations.

The study was conducted in compliance with relevant laws and our institutional guidelines, and was approved by the local ethics committee (reference number 24–195 ANZ, IRB number: IRB00011440, July 8, 2024).

2.2. MRI acquisition and preprocessing

The HCP acquisition protocols and preprocessing pipelines are described in detail elsewhere (Glasser et al., 2013; Smith et al., 2013; Sotiropoulos et al., 2013; Uğurbil et al., 2013). In brief, the rs-fMRI scans were acquired at an isotropic resolution of 2 mm with a TR of 720 ms and a TE of 0.33 ms. Subjects were scanned over four runs (two with left-right phase encoding (PE) and two with right-left PE) with their eyes open, while fixating a cross. Imaging had already been preprocessed, including removal of artifactual components via ICA (FSL FIX, Salimi--Khorshidi et al., 2014). All four rs-fMRI scans of each subject were used for further analysis.

Diffusion MRI was acquired at a resolution of 1.25 mm isotropic with 90 gradient directions at each of three shells with b-values of 1000, 2000 and 3000 s/m^2, respectively. Imaging had as well already been preprocessed and fiber orientations had been estimated using FSL's BedpostX (Jbabdi et al., 2012). Structural scans (3D MPRAGE, TE 2.14 ms, TR 2400 ms, 0.7 mm isotropic) had already been processed via a modified version of Freesurfer's recon-all pipeline (http://surfer.nmr.mgh.harvard.edu/, Dale et al., 1999; Fischl et al., 1999). Functional data was already available in standard space, and non-linear warpfields from structural space to MNI-space had already been generated. These warpfields were used for registration of standard space seeds and targets with dmri data, as the latter were available in structural space.

2.3. Seed and target delineation

For seed delineation, the volume-based multimodal HCP parcellation in MNI space ((Glasser et al., 2016); https://identifiers.org/neurovault.image:30,759) was used to extract bilateral "Piriform" parcels. Additionally, bilateral amygdalae were obtained from the freesurfer segmentation (Freesurfer version 7.4.1) of the MNI152 brain in 1 mm resolution (Fischl et al., 2002). Both regions were added to obtain one large region per hemisphere. These ROI were subsequently extended manually to cover the full potential extent of PC in accordance with a detailed neuroanatomical atlas in MNI-space (Mai et al., 2015), which has been commonly used as a template for segmentation of piriform cortex on MRI images in prior studies (Zhou et al., 2019). This manual extension of bilateral ROI was performed in coronal sections of the MNI brain. In the fronto-mesial direction, ROI delineation was stopped at the mesial boundary of f-PC as delineated from histological data (Mai et al., 2015). In its temporal region, the ROI was extended medially to the most convex point of the medial temporal cortex, corresponding to perirhinal cortex (PRC) and periamygdaloid complex (PAC), covering the entire thickness of the PRC/PAC (Gonçalves Pereira et al., 2005). This deliberate inclusion of neighbouring gray matter was done to probe the mesial extent of PC. In sections further posteriorly, the entire extent of the amygdala was included in the ROI until delineation of this ROI was stopped at the level of the mammillary bodies, as some authors set the caudal limit of PC at this level (Galovic et al., 2019; Gonçalves Pereira et al., 2005; Vaughan and Jackson, 2014). Connectivity based parcellation was conducted both for dMRI and rs-fMRI data. Therefore, the seed-ROI was sampled to 1.25 mm and 2 mm resolution for subsequent analysis of dMRI and rs-fMRI connectivity respectively. After resampling, manual correction of seeds was repeated to ensure a good fit to gray matter regions of interest, resulting in bilateral ROI for both analyses.

The target region for the connectivity analysis was generated by extracting the gray matter ribbon, cerebellar gray matter and subcortical gray matter structures from the 1 mm MNI brain using Freesurfer version 7.4.1 (Dale et al., 1999). The target mask was sampled to the resolution of the respective seeds and the seeds were subtracted from the target. Furthermore, the cortical gray-matter mask was dilated towards the white matter by one voxel to assure coverage of the entire thickness of the cortical ribbon in all cortical areas.

2.4. Connectivity based parcellation

Estimation of connectivity matrices of the respective seed regions was performed using standard space seeds and targets in both modalities. The pipeline established within the recently published toolbox

CBPTools (Reuter et al., 2020) was used to aid connectivity based parcellation, facilitating reproducibility of the reported results. Herein for dMRI data voxelwise seed to target connectivity was estimated using ProbtrackX, generating 5000 streamlines per seed voxel (FSL, Behrens et al., 2007). Correction for streamline length was applied within FSL probtrackX, as is the standard setting for the CBPTools toolbox, as tracking algorithms artificially underestimate connection strengths (i.e., streamline counts) to regions distant from the seed, while the relation of this to the biological decrease in distant connection strengths observed in tract tracing studies is unclear (Sotiropoulos and Zalesky, 2019). For the purpose of connectivity based parcellation, the up-weighting of distant connections allowed for larger contributions of these regions to clustering, as otherwise local connectivity would be driving the analysis predominantly. For rs-fMRI data, each of the four functional runs was z-scored and connectivity matrices were obtained via voxelwise correlations between time courses of seed and target voxels with subsequent fisher z transformation. The four functional connectivity matrices obtained in each subject were then averaged. Spectral clustering was then applied to individual connectivity matrices, assigning each seed voxel to a cluster to obtain an individual parcellation of the seed ROI (eigenvalue decomposition strategy: 'arpack'; labeling method: k-means; number of initiations of k-means with different centroids: 256; affinity matrix construction: 'nearest neighbours'; eigen_tol = 10^{-5}). Nine clustering solutions were investigated (k = 2–10 clusters) per ROI. To obtain a group parcellation, the following steps were followed: first hierarchical clustering using the Hamming distance metric was applied to all individual clustering solutions to obtain reference labels, according to which the arbitrarily labeled individual solutions could then be relabeled. This was done using a permutation approach and the relabeled clustering solution that best matched the reference clustering was kept. Finally, a group parcellation was obtained by labeling each seed voxel according to its most frequent cluster assignment across the group (cf. Reuter et al., 2020).

Furthermore, bimodal parcellations were generated via normalization (min-max-scaling between 0 and 1) and subsequent combination of individual functional and structural connectivity matrices via horizontal stacking, which were then fed into the spectral clustering algorithm. To allow for this procedure, connectivity matrices needed to have equal dimensions in both modalities. Therefore, dMRI-based parcellation of the seed region was repeated using the same seeds and targets as used in the fMRI analysis.

To allow for inference on the likelihood of the obtained parcellations compared to data with unstructured, random connectivity, all individual connectivity matrices were shuffled with subsequent repetition of the above clustering analyses, leading to random parcellations.

2.5. Assessment of validity of group parcellations

Validity of group parcellations was assessed via the average similarity of individual clustering results to the group parcellation as computed via the adjusted rand index (ARI) (Eickhoff et al., 2015). An ARI of 1 indicates the best possible similarity between two parcellations, while an ARI of 0 would indicate random cluster labeling. The lower bound of this measure is −0.5, with negative values indicating especially discordant results (Pedregosa et al., 2011; Steinley, 2004). Reflecting the consistency of clustering results across the study population, this measure was used to compare imaging modalities for their utility in CBP of this region, to analyze whether chance-level in consistency of parcellations was exceeded at all and to select parcellations for further, in-depth analyses. Comparisons of ARI with random parcellations was conducted via paired-sample t-tests with Bonferroni correction for 18 tests (for nine solutions per hemisphere) within each modality.

Further validation was conducted via an analysis of a second cohort of 100 subjects genetically unrelated to each other and to the subjects of the original cohort. The parcellation results of this validation cohort were compared to those of the original cohort. Adjusted Rand Indices between group parcellations were computed. All obtained clustering solutions were evaluated for their separation of the amygdala from the PC and for their cross-subject consistencies (ARI). As there is no single optimal marker for the selection of a best solution among many parcellations of different granularities (Eickhoff et al., 2015), we refrained from the selection of a single clustering solution. Instead, we reported all solutions and subsequently evaluated and discussed consistencies and discrepancies across granularities.

2.6. Analysis of separation of piriform cortex from amygdala

A primary aim of this study was to investigate whether PC could be distinguished from surrounding gray matter via CBP. As the PC neighbors olfactory regions of the amygdala, which some authors included in their previous definitions of PC (Goncalves et al., 2005, Galovic et al., 2019), the distinction of PC from amygdala via these regions' connectivity profiles was analyzed.

For this purpose, regions of interest were delineated within the overall seed region, which are available for review online and which are depicted in Fig. 5. An amygdala ROI was obtained via the freesurfer segmentation of the MNI152 brain and was multiplied with the seed roi and then manually extended by a few voxels to match the extent of the seed. The piriform ROI was obtained via manual extension of the volumetric HCP MMP "Pir" region (Glasser et al., 2016; https://identifiers.org/neurovault.image:30,759) according to a histological atlas (Mai et al., 2015). This region contained small parts that were clearly located in the anterior insula, which we ascribe to the transformation of this surface seed to volume space. Therefore, a small insular part of this region was deleted and labeled as a separate "Insula" ROI.

For each individual subject-level parcellation, each cluster was labeled as either a majority-piriform, a majority-amygdala or a majority-insula cluster, depending on its dice coefficient with the above predetermined regions of interest. Dice coefficients of majority-piriform clusters with the amygdala ROI as well as dice coefficients of majority-amygdala clusters with the piriform ROI were computed and their mean was calculated in each subject, reflecting the individual distinction of PC from amygdala. The group mean of this value was calculated for comparison of the obtained group parcellations as well as for comparisons to random parcellations.

To quantify whether olfactory nuclei of the amygdala are connectionally more similar to piriform cortex than to the amygdala, the same analysis was conducted with modified ROI of PC and amygdala. The hippocampal and amygdala subfield segmentation as implemented in Freesurfer version 7.4.1 was used to identify the medial and cortical nuclei of the amygdala as well as the anterior amygdaloid area. These regions were subtracted from the amygdala ROI and added to the PC ROI with subsequent testing for the separation of both regions according to CBP as implemented above. A paired-sample t-test was conducted to analyze whether the inclusion of olfactory amygdalar nuclei in the definition of the PC ROI improved clustering-based separation of both ROI.

The predetermined ROI of amygdala, PC and insula had been delineated according to the best available knowledge, but their true extent remains uncertain. To address this issue, a group map of mislabeled voxels according to these ROI was created, which granted insight into the frequency with which a voxel was labeled as another region than that of its predetermined ROI. This allowed for descriptive analysis of frequently mislabeled voxels according to CBP, granting insight into regions where either CBP has failed or where the predefined ROI might have been inaccurate. This map was generated for each individual parcellation via saving each 'ectopic' voxel that was located in a region other than the individual majority-cluster that it belonged to. All 100 individual maps were added, obtaining a heatmap indicating how commonly a voxel has been mislabeled according to CBP and the predefined ROI used.

2.7. Descriptive analysis of within-modality connectivity patterns of generated clusters

The connectivity of dmri-derived parcels was explored descriptively (Fig. 11). This analysis was limited to dMRI, as parcellations based on fMRI yielded similar results which were less consistent across the studied population. For each hemisphere, we selected one solution with maximal ARI that separated amygdala, piriform and insula and that had a frontotemporal subdivision within PC. This selection was done in order to highlight potential distinct connectivity profiles of different within-piriform clusters. Images were generated using the program freeview, included within freesurfer (http://surfer.nmr.mgh.harvard.edu/), and ImageMagick (ImageMagick Studio LLC, 2017) for postprocessing. The entire gray-matter was used as the target region and all clusters from the respective clustering solution were selected as seeds. Seed to target-connectivity was computed for each cluster and each subject using ProbtrackX (Behrens et al., 2007). Resulting seed-to-target connectivity maps were averaged across all subjects, so that one map of gray matter streamline-counts resulted per parcel. Streamline counts were corrected for streamline length as outlined in Section 2.4. FSL's *find_the_biggest* method was then used to highlight gray-matter voxels that had the strongest connectivity with each respective cluster. The resulting volumetric maps were projected to the surface for visualization using freesurfer's *mri_vol2surf* tool.

2.8. Differences in functional connectivity across clusters obtained via diffusion MRI

Differences in whole-brain functional connectivity across clusters located within the piriform cortex were assessed. For this analysis, clusters located in PC as obtained from bilateral dMRI-based solutions (at 1.25 mm isovoxel resolution) were downsampled to the 2 mm isovoxel resolution of the fMRI scan, and the functional connectivity of each cluster with the entire gray matter was computed. The same solutions as used for the descriptive analysis from Section 2.7 were selected for this analysis. Seed-based connectivity analysis was conducted using the python package nilearn, which relies on the machine learning package scikit-learn (Abraham et al., 2014; Pedregosa et al., 2018). Three seed-based, fisher-z-transformed correlation maps were obtained bilaterally, corresponding to three within-PC seeds analyzed (i.e., f-PC, dorsal t-PC (dtPC) and anterior and ventrotemporal-PC (avtPC). For each z-map, a one-sample *t*-test was conducted in FSL randomize with 50k permutations and threshold-free cluster enhancement to obtain t-maps of significant connectivity (Fig. 13A). Bonferroni correction for six comparisons was applied.

Additionally, six contrasts resulted per hemisphere: f-PC > dt-PC, f-PC > avt-PC, dt-PC > f-PC, dt-PC > avt-PC, avt-PC > f-PC and avt-PC > dt-PC. Paired two-sample permutation *t*-tests were conducted using FSL *randomise* with 50k permutations with threshold free cluster enhancement and FWE-correction for multiple testing. Additionally, Bonferroni correction for twelve tests was implemented, so that the alpha for the resulting statistical maps was set to $p = 0.0042$.

In addition to seed-based connectivity maps and the statistical t-maps of the above contrasts (Figure S17), also a binary map was generated that shows all regions where both left and right f-PC exhibit significantly stronger functional connectivity compared to both respective ipsilateral dt-PC and avt-PC. This map therefore summarizes those regions to which f-PC had stronger connections than f-PC and dt-PC, irrespective of the hemisphere (Fig. 13B).

3. Results

Parcellations of a large ROI encompassing the piriform cortex and the adjacent amygdala were generated at granularities of $k = 2$–10 clusters from both rs-fMRI and dMRI. Additional bimodal parcellations were computed from both modalities at each granularity. Validity of parcellations was assessed via the mean Adjusted Rand Index (ARI) as a measure of similarity between individual and group parcellations (cf. Methods section 4.5). The distinction between PC and amygdala of a group parcellation was quantified via the mean of dice coefficients of majority-piriform clusters with predefined amygdala and vice versa at the individual level (cf. Methods Section 2.6).

3.1. Parcellation based on structural connectivity

3.1.1. Right hemisphere

The $k = 2$ solution clustered the seed into an antero-lateral and a postero-medial region. At $k = 3$, an anterior and insular cluster was detected in addition to an amygdalar cluster as well as one cluster covering the c-shaped cortex around the endorhinal sulcus (ES) overlying the frontal PC (f-PC) and temporal PC (t-PC) (Mai et al., 2015). At $k = 4$, the amygdala was divided into medial and lateral clusters. The $k = 5$ solution added a lateral cluster at the boundary of t-PC and f-PC. Lateral anterior parts of the seed were now grouped with the insula, while antero-medial parts were grouped with t-PC and parts of f-PC. The 6-cluster solution yielded a frontobasal cluster covering f-PC, the aforementioned lateral cluster at the frontotemporal boundary within the t-PC (from here on: dorsal t-PC, dt-PC), as well as the anterior cluster encompassing ventral t-PC, frontobasal regions and parts of the planum temporale anterior to the limen insulae (anterior and ventrotemporal PC, avt-PC; colored in red). At $k = 7$ a third amygdalar cluster was added, while at $k = 8$ no additional cluster emerged at the group level, indicating high variability in its location across subjects. The 9-cluster solution contained two additional clusters of negligible extent within the dt-PC and the amygdala. The ten-cluster solution contained two separate clusters in the dt-PC region, while the dorsal extent of the avt-PC cluster became smaller.

3.1.2. Left hemisphere

The two-cluster solution was analogous to its right-sided homologue (Fig. 2). The three-cluster solution contained an additional amygdalar cluster, and the 4-cluster solution added a cluster covering frontal and dorsotemporal PC, which became separated into dorsotemporal and frontal PC clusters at $k = 5$. At $k = 6$ clusters, the insula (depicted in yellow) was separated from the anterior and ventrotemporal PC cluster (avt-PC, depicted in red). The 7-cluster solution added a third cluster in the amygdala, and the 8-cluster solution showed an additional very small cluster in the caudal amygdala. At $k = 9$, only eight clusters were evident at the group level with now four clusters present in the amygdala. The ten-cluster solution revealed a split of the insular part of the ROI into rostral and caudal subdivisions.

Overall, dMRI-based connectivity-based parcellation consistently resulted in the distinction of PC from insula and amygdala. Delineation of an anterior frontotemporal (avt-PC), a posterotemporal (dorsal temporal PC, dt-PC) as well as a posterofrontal subdivision (frontal PC, f-PC) within PC was observed with consistency and bilaterally.

Parcellations were highly consistent across individuals especially in solutions with lower numbers of clusters, and subdivisions within PC remained similar with increasing numbers of clusters $> k = 5$. Individual to group similarity significantly exceeded chance for all clustering solutions (Fig. 3).

3.1.3. Separation of piriform cortex from amygdala

Separation of piriform cortex from amygdala was computed in each subject-level parcellation via 1) labeling clusters as either majority piriform clusters, majority amygdala or majority insula clusters according to their dice coefficients with predefined ROI (cf. Methods Section 2.6), with 2) subsequent computation of dice coefficients of majority PC clusters with the amygdala ROI and vice versa, using the mean of both dice coefficients as a measure of separation. The separation of PC from amygdala significantly exceeded chance and the overlap between these regions was small across hemispheres and clustering

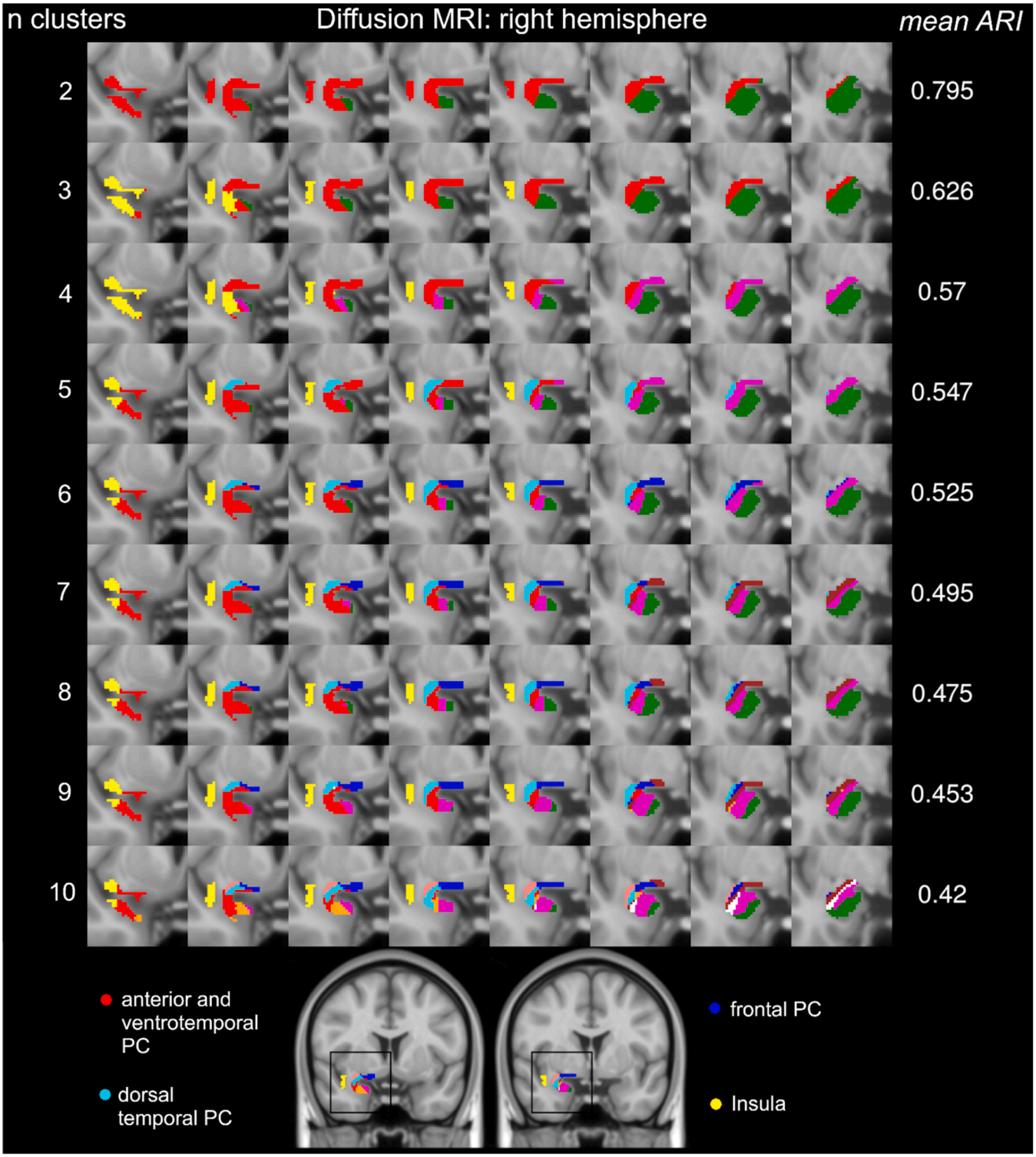

Fig. 1. Coronal slices of clustering results of the right region of interest based on structural connectivity. Progression from left to right indicates progression from anterior to posterior, while granularity of clustering solutions increases from top ($k = 2$) to bottom ($k = 10$). Numbers on the right indicate mean adjusted rand index (ARI). Background image: T1 standard space image at 1 mm isovoxel resolution (MNI152).

solutions (Fig. 4a). Distinctions between these regions were less accurate when defining olfactory regions of the amygdala as PC rather than as amygdala (Fig. 4b) for the assessment of their separation.

To illustrate which regions drove potential errors in separation of PC from amygdala by CBP and to highlight potential regions where the partly manually defined ROI of PC and amygdala might have been erroneous, heatmaps of voxelwise mislabeling frequencies were generated (Fig. 5). Especially mesial aspects of the temporal bank of the endorhinal sulcus contained voxels with high frequencies of discrepancies in labelling between CBP and predefined ROI, with CBP estimating the mesial extent of PC as smaller than the predefined ROI.

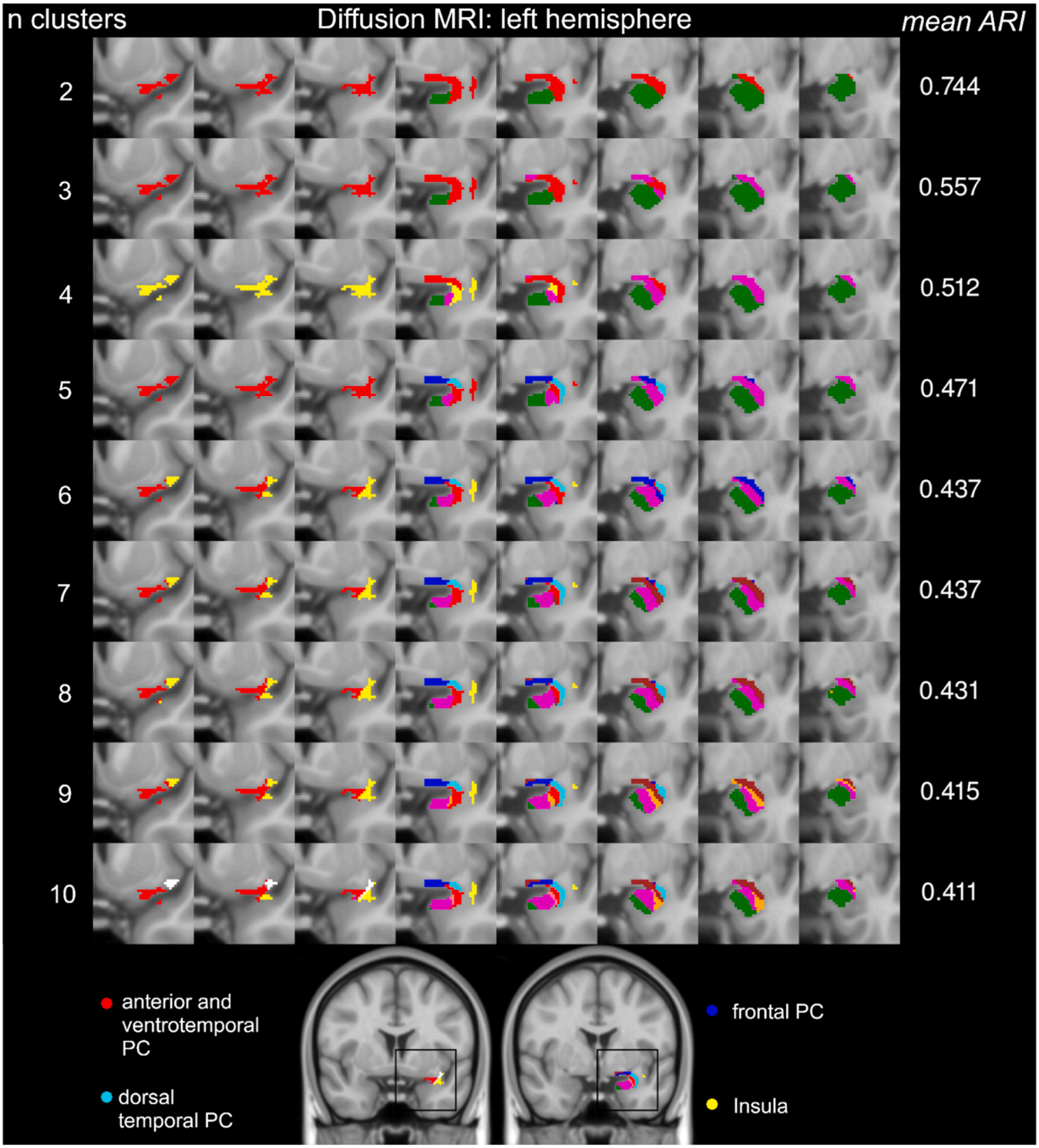

Fig. 2. Coronal slices of clustering results of the left region of interest based on structural connectivity. Progression from left to right indicates progression from anterior to posterior, while granularity of clustering solutions increases from top ($k = 2$) to bottom ($k = 10$). Numbers on the right indicate mean adjusted rand index. Background image: T1 standard space image at 1 mm isovoxel resolution (MNI152).

3.2. Parcellation based on functional connectivity

3.2.1. Right hemisphere

The 2-cluster solution separated few insular voxels from the remaining seed ROI. At higher granularities, a cluster in the f-PC (from $k = 3$ on) and a dorsoventral subdivision in the medial amygdala emerged (from $k = 4$ on). At $k = 6$, the distinction of the insular cluster was more marked and a cluster similar to the anterior and ventrotemporal PC cluster observed in the dMRI parcellations emerged (red color in Fig. 6). This cluster, as opposed to dMRI-based solutions, extended into lateral amygdala in this modality. Both the f-PC and avt-PC clusters remained visible in all granularities up to the 10-cluster solution. Finer parcellations added a dorsoventral division in the insular part of the seed, as well as further subregions within the amygdala. A dorsotemporal correlate of

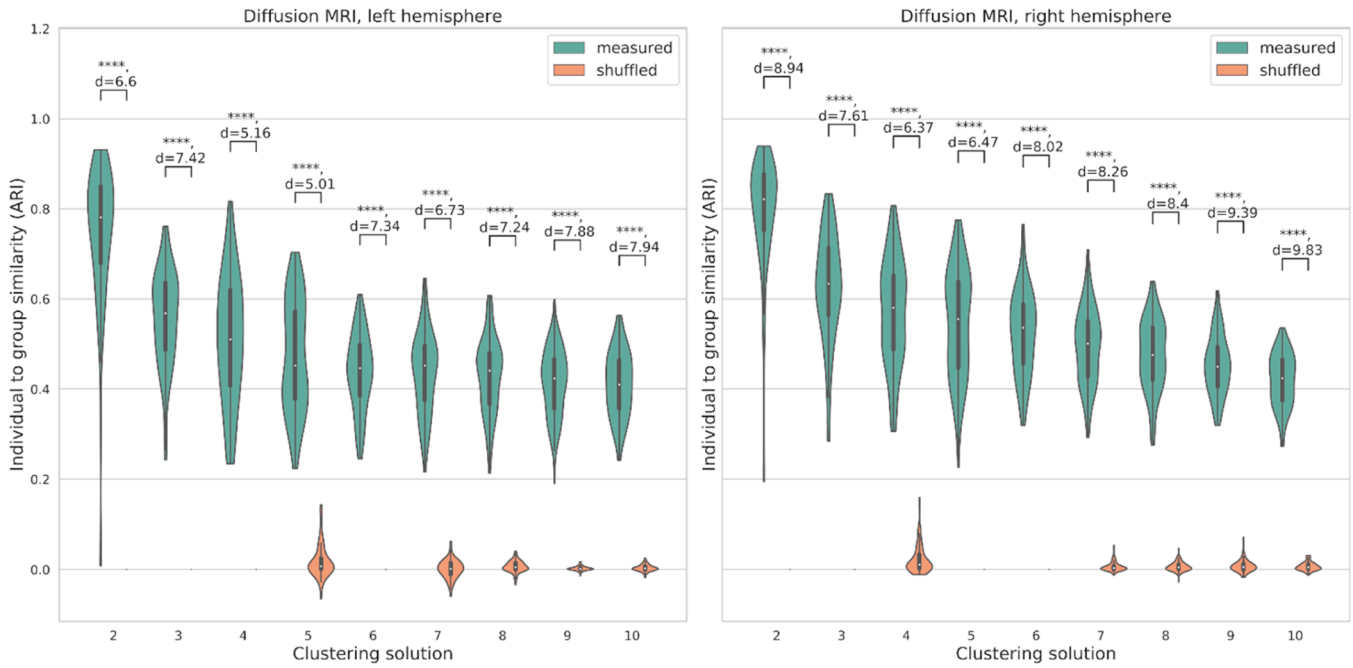

Fig. 3. Comparison of adjusted rand indices with those obtained from parcellations generated from shuffled connectivity matrices. For each parcellation, a paired sample *t*-test was conducted; **** = $p < 0.0001$ (Bonferroni corrected), d indicates Cohen's d.

the dMRI-based dt-PC seed at the mesial frontotemporal junction was not detected.

3.2.2. Left hemisphere

Parcellations on the left hemisphere were similar to their right hemispheric counterparts. On the left side, however, a cluster at the mesial frontotemporal junction (cyan color in Fig. 7) was observed in the 5-cluster solution and onwards, similar to the dt-PC cluster observed in dMRI based parcellations. Contrary to the right hemisphere, no dorsoventral subdivision within the insular part of the ROI was observed. An avt-PC parcel similar to the right hemisphere and to dMRI-based parcellations was detected in the 6-cluster solution only, as its frontobasal and temporal parts formed separate subregions from the 7-cluster solution onward.

Overall, results from functional parcellations showed larger inter-individual variability compared to dMRI based parcellations, leading to lower ARI. However, some subregions were parcellated with consistency, such as the f-PC, as well as distinctions of insula from PC and of temporal piriform cortex from amygdala to some extent. The similarity of individual parcellations to the group parcellations presented in Figs. 6 and 7 significantly exceeded individual-to-group similarities based on random connectivity (Fig. 8).

3.2.3. Separation of piriform cortex from amygdala based on functional connectivity

Separation of PC from amygdala was achieved with lower dice coefficients than chance while overlaps between both regions remained large (Fig. 9A). Contrary to results from dMRI-based parcellations, less consistent results were obtained when comparing CBP-based separation of amygdala and PC using both alternative definitions of PC (Fig. 6B). Here, distinctions of PC from amygdala were better when cortical amygdala was defined as amygdala instead of as PC only from the 5-cluster solution onwards and with low effect sizes. Bilateral 2-cluster solutions yielded contrary results.

Distinctions of both regions were less accurate than those based on dMRI (Fig. 10).

3.3. Bimodal parcellations

Bimodal parcellations were generated via normalization and horizontal stacking of individual functional and structural connectivity matrices, with subsequent spectral clustering as conducted in the above analyses (c.f. Methods Section 2.4). Bimodal parcellations were similar to those derived from dMRI alone (Table S1), while no increase in ARI compared to dMRI-based parcellations was observed (supplementary figures S1–2).

3.4. Validation cohort

To assess the reliability of our results, the same analyses were repeated in an additional sample of 100 unrelated subjects from the HCP, who were also unrelated to our original sample. Group parcellations of both cohorts showed good agreement (Table 1) with decreasing similarity as granularity of parcellations increased. Individual to group similarities, separations of amygdala from PC as well as clusters obtained within PC were highly similar across cohorts (Supplementary Figures S7 to S16.

3.5. Seed-based connectivity analysis of generated clusters

In this section connectivity profiles of clusters from dMRI-based parcellations, which showed the highest ARI among the tested modalities, are illustrated descriptively (Fig. 11). For this purpose, the bilateral 7-cluster solutions were selected, as both parcellations 1) contained separate clusters within f-PC, posterodorsal t-PC and anterior and ventrotemporal PC; 2) contained a separate insular region and 3) had the highest mean ARI among ipsilateral parcellations that fulfilled the criteria 1) and 2).

The anterior PC-cluster extending into ventral t-PC posteriorly showed the strongest connections among all parcels with parts of the orbitofrontal cortex, anterior insula, the planum temporale, and with patches of the precentral gyrus and mesial prefrontal cortex (red). The posteriorly located f-PC cluster had strong connectivity with bilateral basal ganglia. In the left-sided parcellation it also exhibited strong connectivity with lateral orbitofrontal cortex, ipsilateral pre- and

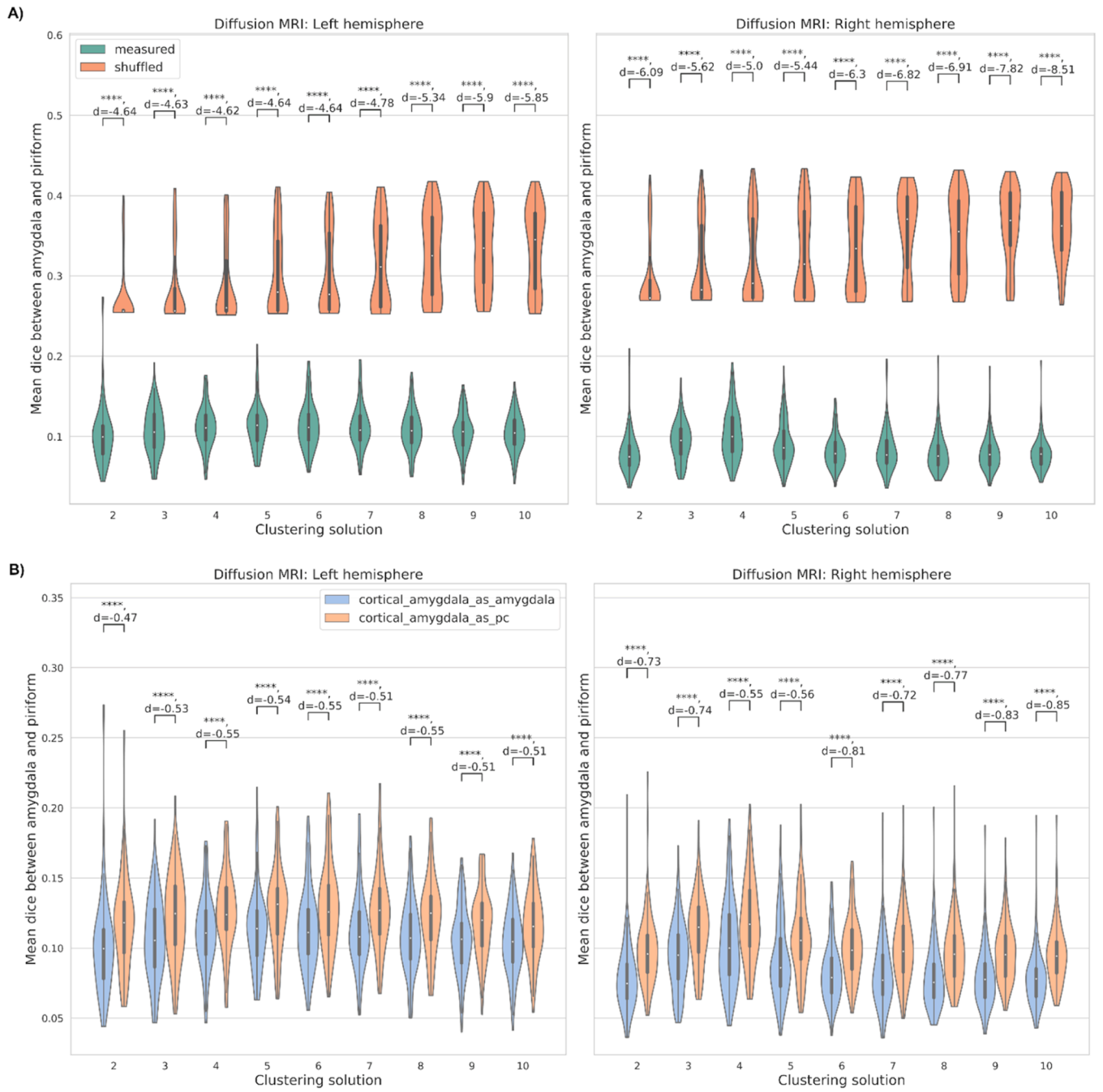

Fig. 4. A) Distinction of amygdala from piriform cortex via dMRI-based CBP as compared to parcellations obtained from shuffled connectivity data of the same individuals (paired-sample *t*-test, ****=$p < 0.001$, Bonferroni corrected, d indicates Cohen's d). B) Comparison of this distinction with distinctions achieved by an alternative definition of PC including olfactory amygdala in the predefined PC ROI (cortical_amygdala_as_pc); paired sample *t*-test, ****=$p < 0.001$, Bonferroni corrected.

postcentral gyri and dorsolateral prefrontal cortex, while its right-sided counterpart was connected mainly to cortex in its immediate vicinity and the basal ganglia (blue). The postero-dorsal t-PC cluster bilaterally had extensive connections that were the strongest among all parcels, notably with the cingulate and further parts of medial prefrontal cortex, orbitofrontal cortex, the cuneus and occipital pole, basal temporal lobes and the inferior temporal gyri. On the right side, it also had strong connections with the precentral gyri.

Fig. 12 shows the distribution of streamline-counts shared between voxels projected to the cortical surface and the respective piriform subregions used in the above analysis.

3.6. *Differences in functional connectivity across dMRI-derived clusters*

Functional connectivity profiles of clusters defined via dMRI were computed and significant connections were calculated using one-sample *t*-tests (Fig. 13A).

After the above descriptive depiction of cluster-wise connectivity profiles, we explored potentially distinct functional connectivity patterns within the PC that might hint at different functions of its subregions. Paired two-sample permutation-tests for differences in functional connectivity across dMRI-defined PC-subclusters - as obtained from bilateral 7-cluster solutions - were conducted (Fig. 13B). Here, bilateral f-PC showed significantly stronger connectivity than both

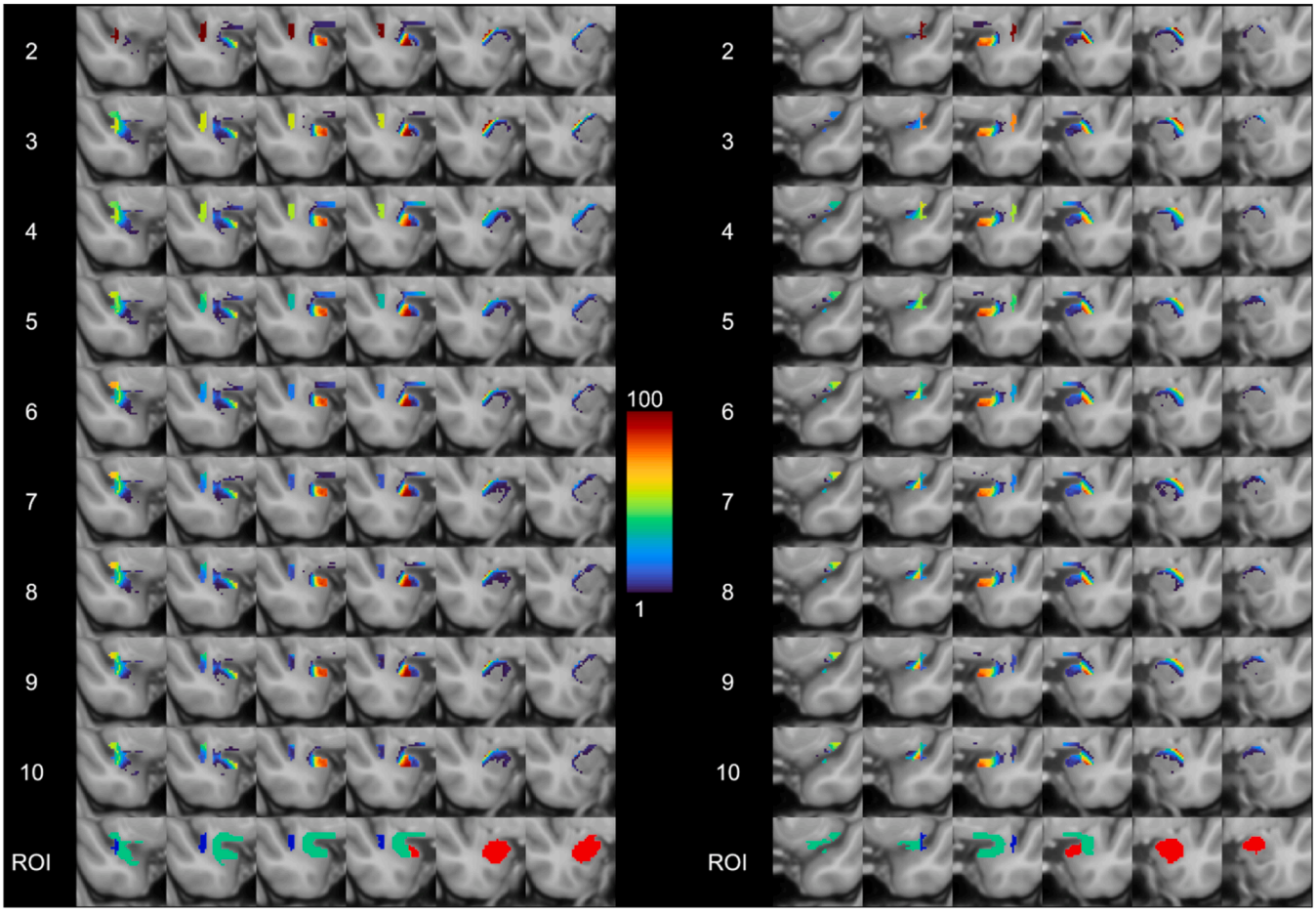

Fig. 5. Colormaps of discrepancies in labeling of voxels between dMRI-based CBP and predefined ROI of amygdala (red), PC (green) and insula (green) shown in the last row. Granularity of clustering solutions increases from top to bottom and progression of slices from left to right indicates progression from anterior to posterior. Intensity of voxels indicates count of subjects (range 1–100) in whom the respective voxel showed a discrepancy in labeling between CBP and predefined ROI. Background image: T1 standard space image at 1 mm isovoxel resolution (MNI152).

dorsal t-PC and avt-PC with bilateral supramarginal gyri, dorsolateral prefrontal cortex and the basal ganglia (Fig. 13B). Both avt-PC and dt-PC did not show significantly stronger connectivity compared to the respective remaining PC subregions with consistency across hemispheres.

Furthermore, functional connectivity of the piriform cortex was compared to that of the amygdala statistically. Clusters within the piriform cortex from bilateral 7-cluster solutions were merged to form bilateral PC ROI, and bilateral amygdala ROI were created analogously.

Bilateral amygdalae did not exhibit stronger connectivity than the piriform cortex, except for self-connections. Piriform cortices, however, bilaterally exhibited stronger connectivity than the amygdalae with extensive brain regions, especially with bilateral occipital cortices, supramarginal gyri, posterior cingulate cortex and dorsolateral prefrontal cortex (Figure S18).

4. Discussion

We demonstrated that the human PC and the amygdala can be distinguished based on their connectivity profiles alone. Reliable parcellations with consistent subregions within the piriform cortex were observed based on diffusion MRI, and partial agreement with functional parcellations, especially in the frontal PC, was observed.

4.1. Clustering solutions

Parcellations based on dMRI were more reliable than those produced via fMRI, as functional parcellations showed larger interindividual variability.

In dMRI-based parcellations, the PC was separated from the adjacent amygdala with accuracy and consistency across clustering solutions and hemispheres. We showed that the medial (MeA) and cortical amygdala (CoA) and anterior amygdaloid area (AAA) do not appear to be related to the piriform cortex. This contrasts with a recent definition of the piriform cortex as a “piriform-cortical amygdala area” (PCA) used in clinical studies in the context of epilepsy surgery (Borger et al., 2022, 2021; Galovic et al., 2019). Here, the resection of at least 50 % of this PCA (which included MeA, CoA and parts of AAA) was associated with a favorable outcome in patients with temporal lobe epilepsy. The clinical implications of different subregional definitions of the piriform cortex are of interest, as finer-grained parcellations of the PC may provide smaller, more specific surgical targets of interest in the future and warrant further research. On the other hand, a stricter definition of the PC may also raise the question whether the resection of the PC can be associated with postoperative seizure-freedom based on these studies at all, or whether just a more complete resection of the olfactory amygdala would have been sufficient.

Functional parcellations supported this dMRI-based finding only in parcellations with granularities of 5 clusters and higher, and with small effect sizes.

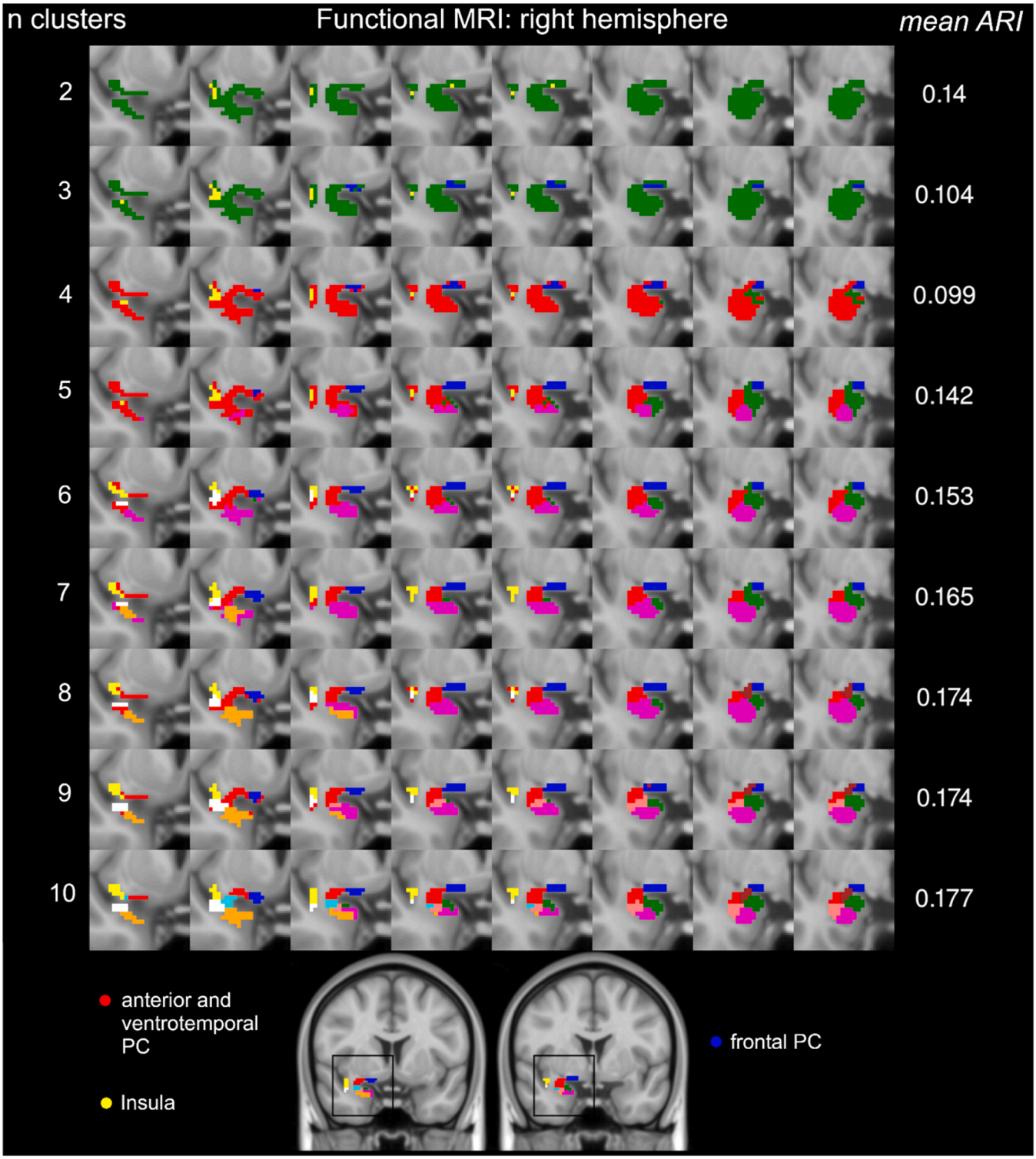

Fig. 6. Coronal slices of clustering results based on functional connectivity of the right ROI. Progression from left to right indicates progression from anterior to posterior, while granularity of clustering solutions increases from top ($k = 2$) to bottom ($k = 10$). Numbers on the right indicate mean adjusted rand index. Images in the last row show the location of the ROI with the 10-cluster solution depicted as overlay. Background image: T1 standard space image at 1 mm isovoxel resolution (MNI152).

We confirmed previous reports of a fronto-temporal division within the PC (Allison, 1954; Mai et al., 2015; Zelano et al., 2005; Zhou et al., 2019), which was consistent across modalities, hemispheres and clustering granularities. Tract-tracing studies in macaque monkeys support this concept of connectionally separate frontal and temporal subdivisions within the PC (Carmichael et al., 1994). In contrast, in rodents, the piriform cortex is divided into anterior and posterior subdivisions, with underlying distinct cellular responses to odors (Courtiol et al., 2019; Litaudon et al., 2003), distinct connectivity to olfactory and remote cortial regions (Haberly, 2001) and an increased density of GABAergic interneurons at their transition zone (Löscher et al., 1998). Interestingly, in dMRI-based solutions a dorsal cluster at the

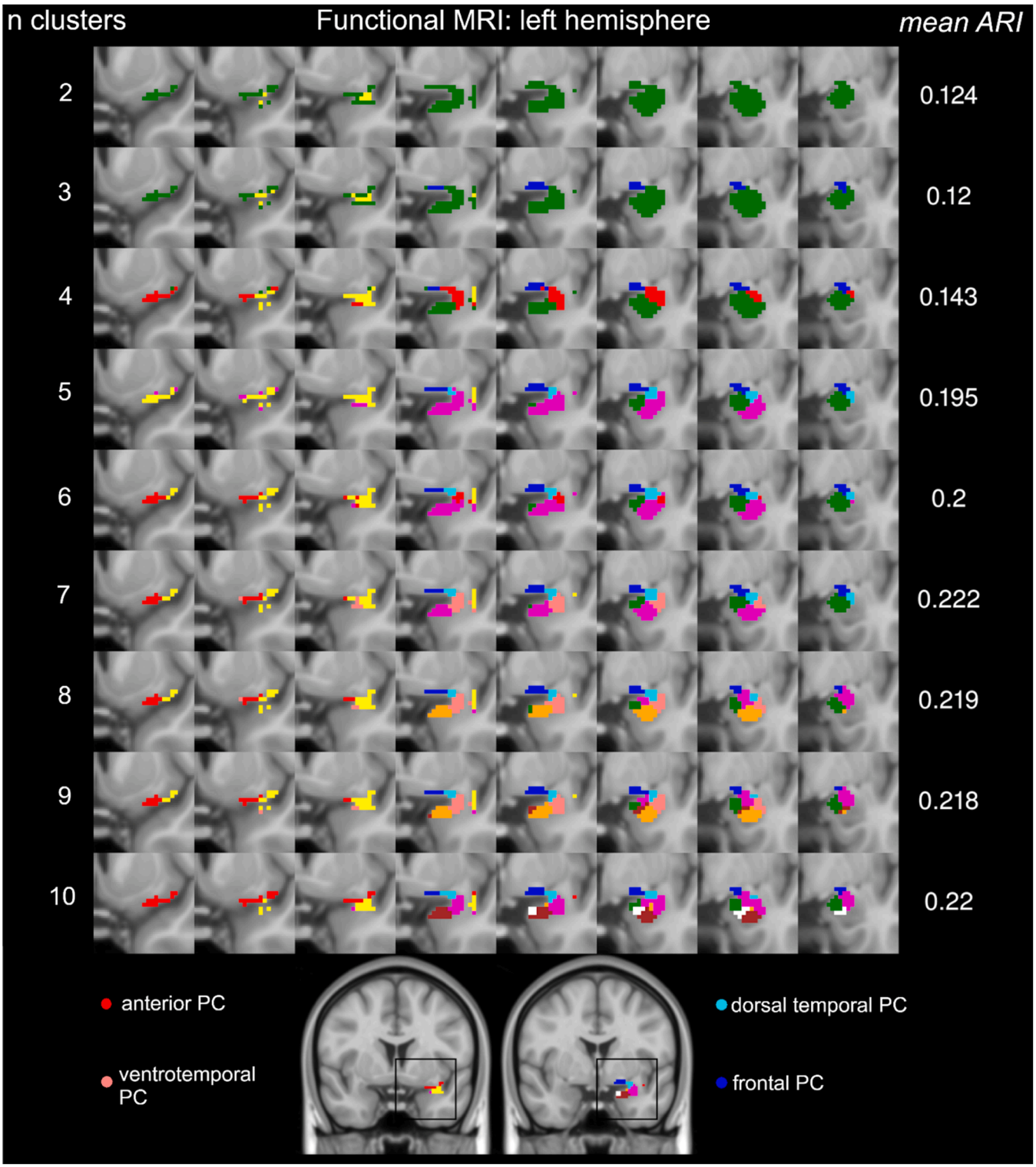

Fig. 7. Coronal slices of clustering results based on functional connectivity of the left ROI. Progression from left to right indicates progression from anterior to posterior, while granularity of clustering solutions increases from top ($k = 2$) to bottom ($k = 10$). Numbers on the right indicate mean adjusted rand index. Images in the last row show the location of the ROI with the 10-cluster solution depicted as overlay. Background image: T1 standard space image at 1 mm isovoxel resolution (MNI152).

fronto-temporal boundary as well as an antero-ventral cluster were observed bilaterally. The latter extended anteriorly beyond the limen insulae into temporal and frontobasal cortices which have been labeled as "anterior piriform cortex" by some authors (Mai et al., 2015). In some functional parcellations, a similar cluster was observed as well. It is worth noting that regions rostral to the limen insulae have not been investigated in studies that probed the relevance of resection of the PC in epilepsy surgery (Galovic et al., 2019; Borger et al., 2021). In rats, kindling of the anterior PC can lead to its epileptogenic transformation and to the spread of seizures to the posterior PC and further regions (Haberly, 2022). We therefore encourage the consideration of anterior aspects of the piriform cortex, such as the region delineated in the

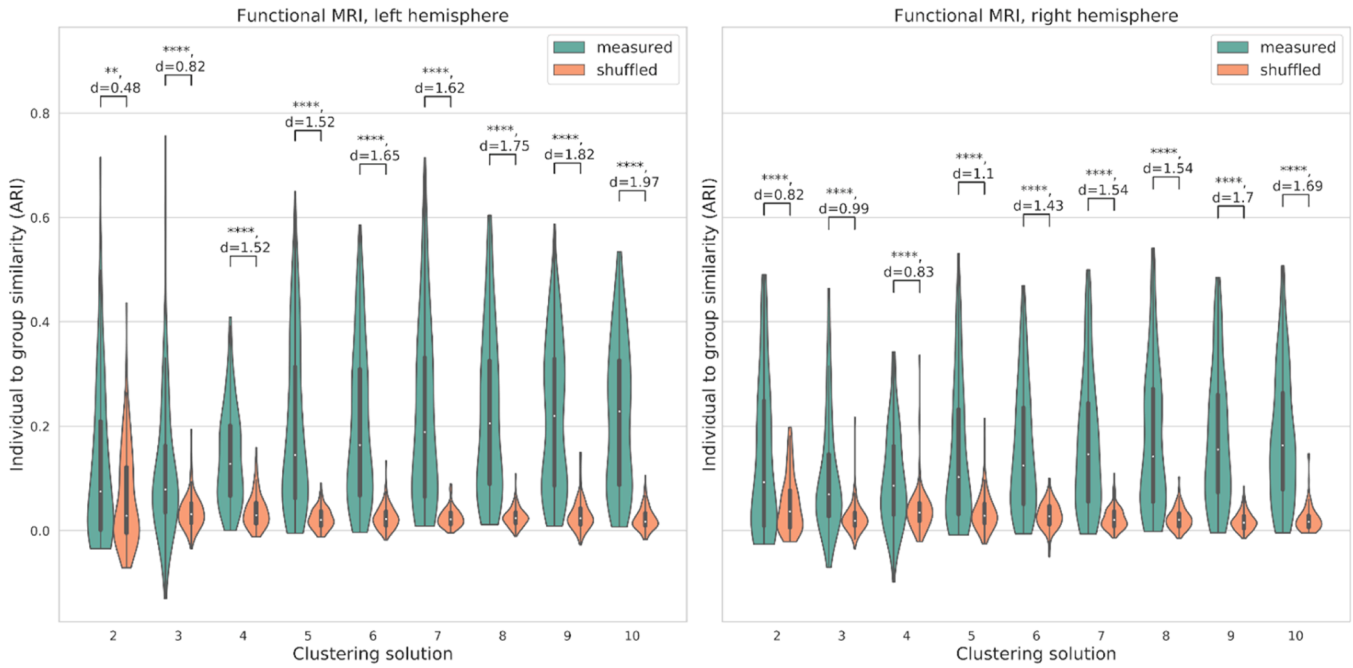

Fig. 8. Comparison of adjusted rand indices with those obtained from parcellations generated from shuffled connectivity matrices. For each parcellation, a paired sample *t*-test was conducted; * = $p < 0.05$; ** = $p < 0.01$; ***=$p < 0.001$; **** = $p < 0.0001$; ns = not significant (Bonferroni corrected for 18 tests); d indicates Cohen's d.

present study, in investigations into the role of the piriform cortex in human epilepsies. This rostral subregion extending into ventral t-PC has not been described before, and future studies into the functional relevance of this connectionally delineated region will be of great interest. In healthy subjects, the anterior piriform cortex has been shown to generate odor-specific activity in expectation of odors (Zelano et al., 2011) and seems, in contrast to posterior PC, to be sensitive to their hedonic tone (Gottfried et al., 2002). Posterior PC has been demonstrated to respond to odors irrespective of their valence and has been implicated in the quality coding of odors (Howard et al., 2009).

Especially in the temporomesial aspect of the ROI, CBP has consistently "mislabeled" parts of predefined PC as amygdala (Fig. 5). In this definition of PC we employed, PC had been extended to the tip of the ambiens gyrus including periamygdaloid complex, as no boundary of these structures was evident within the atlas we used (Mai et al., 2015), and receded laterally in its posterior portions. Histologically, the transition between amygdaloid areas and the overlying piriform cortex has been found to be smooth, with "*cellular continuity*" of strands of pyramidal cells extending from one region into the other (Crosby and Humphrey, 1941). In nearly all subjects, CBP did not agree with this mesial extent of the PC in our predefined ROI, leading us to question our manual delineation of subregions in this part of the ROI. It may be that this disagreement reflects a connectional distinction between PC and PAC; however, this remains somewhat speculative as the extent and function of the human PAC remain poorly understood (Lane et al., 2020). Histological studies investigating the extent of both structures in humans are scarce and therefore of great interest in the future. Overall, plausible, bilateral dMRI-based parcellations of the PC have been obtained which correspond well to previous studies from different modalities, while the subdivision of the t-PC in two separate subregions with its ventral subdivision being part of the anterior PC was a surprising finding which has not been described before.

4.2. Connectivity profiles of the obtained clusters

The frontal PC showed dominant functional and structural connectivity with motor regions such as bilateral basal ganglia, which has also been reported in a previous fMRI study (Zhou et al., 2019). Meanwhile, all PC subregions showed strong functional connectivity with extensive visual regions, and evidence that olfaction and visual information may be integrated for certain motor tasks such as grasping for food has been found before (Yang and Wang, 2020).

Integration of olfactory and visual information in the PC is also supported by previous findings showing that congruent visual and olfactory information enhance odor detection (Gottfried and Dolan, 2003), and that emotional visual information can modulate piriform activity and valence perception (Schulze et al., 2017).

The supramarginal gyri, which had dominant functional connectivity with the f-PC, have been demonstrated to be activated during olfactory recognition memory tasks (Cerf-Ducastel and Murphy, 2006) and had reduced volume in anosmic patients (Bitter et al., 2010). Therefore, it is possible that the supramarginal gyri form a relevant node in the olfactory network.

Posterior temporal piriform cortices (dt-PC) formed strong and extensive structural connections across multiple regions, but this was not reflected in its functional connectivity, where the dt-PC had less extensive connections as compared to avt-PC and f-PC. The biological substrate of this discordance between modalities remains unclear and requires further investigation.

4.3. Limitations

A limitation of connectivity-based parcellation studies is the selection of the best parcellation among many granularities, as there is no single optimal marker for the selection of such a parcellation (Eickhoff et al., 2015). We therefore refrained from selection of a single parcellation as the "best" result, but rather reported on all analyzed parcellations and their consistencies. Still, the average ARI, as an external validation criterion for clustering results, was obtained as a measure of the fit of the group parcellation to the individual results from the entire population, also allowing for cross-modal comparisons. Another potential limitation is that the seed ROI and predefined piriform ROI were manually extended according to an anatomical atlas after their initial automated generation, which may have introduced slight errors in, e.g.,

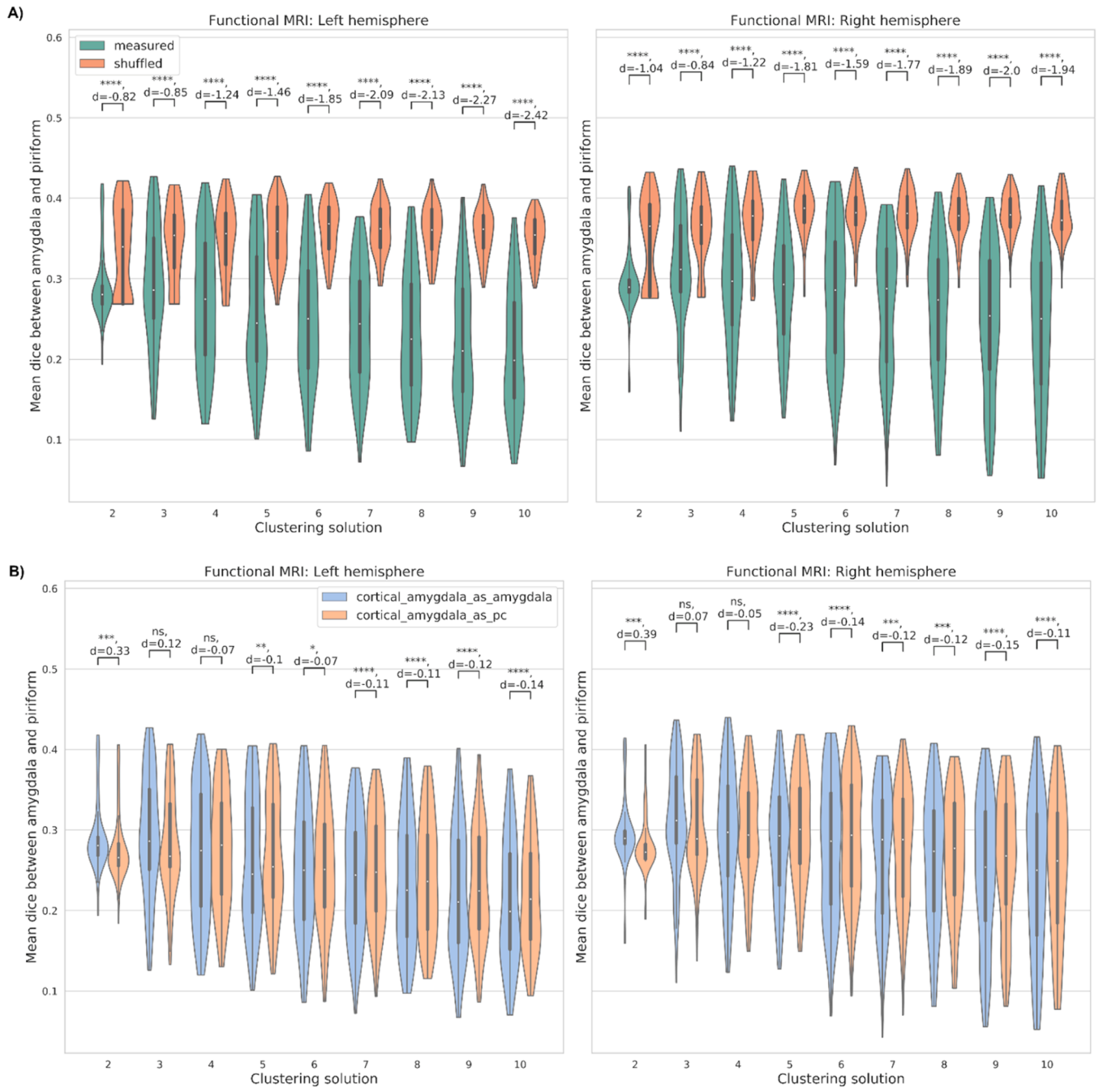

Fig. 9. A) Comparison of the distinction of amygdala from PC based on fMRI-based parcellations vs. parcellations obtained from shuffled connectivity matrices B) Comparison of this distinction with distinctions achieved by an alternative definition of PC including olfactory amygdala in the predefined PC ROI (cortical_amygdala_as_pc). Paired sample *t*-test, Bonferroni corrected for 18 comparisons. * = $p < 0.05$; ** = $p < 0.01$; ***=$p < 0.001$; **** = $p < 0.0001$; ns = not significant; d indicates Cohen's d.

the boundary of the PC with amygdala. Therefore, as the dice indices between the amygdala and the piriform cortex relied on in part manually delineated subregions, these measures could be influenced by potential errors in manual delineation. However, as there are no automated methods for the delineation of PC available to date, this approach (in accordance with a histological atlas, Mai et al. 2015) was without alternative.

It remains unclear whether individual parcellation results could be used for reliable individual, data-driven delineations of a subject's PC. To test this, functional studies of the obtained regions of interest within the PC would need to be conducted.

We extensively studied the multimodal connectivity of a large seed region at the mesial frontotemporal junction, which included at least three different brain regions (insula, amygdala, PC), all of which were separated with accuracy. However, further extension of the seed region, especially rostrally, could have led to a larger estimation of the piriform cortex. We stopped the seed delineation at the rostral boundary of the "Pir" region of the Glasser 2016 multimodal parcellation (Glasser et al., 2016) in order not to (a) introduce bias via further manual delineation and (b) because the rostral boundary of the seed would have needed to be extended arbitrarily for the lack of an accepted rostral landmark. However, therefore, the PC might extend further rostrally than indicated by the produced parcellations.

We were able to show distinct connectivity profiles of subregions

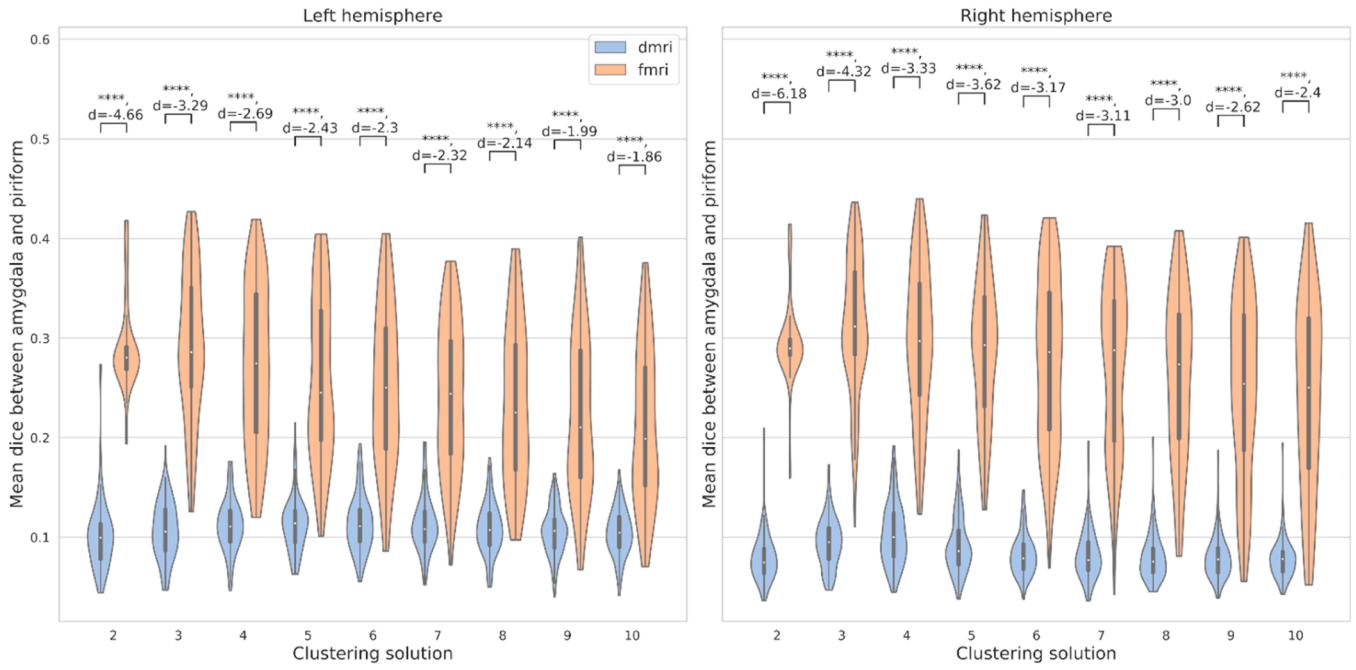

Fig. 10. Comparison of the distinction of amygdala from PC based on fMRI-based parcellations vs. dMRI-based parcellations. Paired sample *t*-test, **** = Bonferroni corrected $p < 0.0001$, d indicates Cohen's d.

Table 1
Similarity (adjusted rand index) between group parcellations from the original cohort compared to the validation cohort.

dmri				*fmri*				*Bimodal*			
left hemisphere		*right hemisphere*		*left hemisphere*		*right hemisphere*		*left hemisphere*		*right hemisphere*	
solution	**ARI**	**solution**	**ARI**	**solution**	**ARI**	**solution**	**ARI**	**solution**	**ARI**	**solution**	**ARI**
2	0.93	**2**	0.96	**2**	0.53	**2**	0.39	**2**	0.93	**2**	0.96
3	0.94	**3**	0.76	**3**	0.09	**3**	0.32	**3**	0.76	**3**	0.88
4	0.91	**4**	0.76	**4**	0.31	**4**	0.2	**4**	0.67	**4**	0.91
5	0.8	**5**	0.68	**5**	0.28	**5**	0.23	**5**	0.81	**5**	0.75
6	0.67	**6**	0.79	**6**	0.47	**6**	0.22	**6**	0.5	**6**	0.8
7	0.73	**7**	0.77	**7**	0.53	**7**	0.22	**7**	0.66	**7**	0.79
8	0.77	**8**	0.68	**8**	0.57	**8**	0.28	**8**	0.71	**8**	0.78
9	0.73	**9**	0.69	**9**	0.51	**9**	0.33	**9**	0.65	**9**	0.84
10	0.61	**10**	0.68	**10**	0.44	**10**	0.47	**10**	0.61	**10**	0.67

within the PC, which were in part in accordance with previous results (Zhou et al., 2019). Based on our data, the functional relevance of these distinctions within the PC can only be speculated about. Analyses of potentially distinct functions of the detected subregions are therefore of great interest in the future.

Finally, we would like to emphasize that the nomenclature of subclusters (e.g., f-PC) was based on their visual concordance with atlas- and histology-based regions reported in the rather sparse literature (Allison, 1954; Mai et al., 2015). This requires some caution in interpretation, as it is not guaranteed that all voxels of a cluster labeled as a particular region lie within that region.

5. Conclusion

Connectivity-based parcellations conducted with diffusion MRI data confirmed that the piriform cortex and the amygdala, including its olfactory regions MeA and CoA, are functionally separate entities within the brain. The exact location of the boundary between temporal PC and periamygdaloid complex, however, remains blurred. The division of the piriform cortex in frontal and temporal subregions - a subdivision which has been reported before based on histological findings - consistently emerged in parcellations across modalities, hemispheres and granularities. We could further validate the functional distinction of these subregions by demonstrating significant differences in connectivity with distinct cortical and subcortical loci between f-PC and t-PC. We produced the first diffusion-MRI based parcellations of the piriform cortex, and our findings from this modality suggest the potential existence of two connectionally distinct dorsal and ventral subregions within the temporal PC, with the latter also encompassing the anterior PC. Future research into the potential biological significance of this finding will be of great interest.

Overall, our results contribute to the otherwise scarce understanding of the architecture and the boundaries of the human piriform cortex. We made all parcellations obtained in this work publicly available to facilitate further research on the role of the piriform cortex in health and disease.

Funding

Felix Zahnert was funded by the German chapter of the International League against Epilepsy (DGfE) via an Otfrid Foerster Grant. Felix Zahnert received further funding by the Clinician Scientist program of the Philipps University Marburg and the University Hospital of Marburg. Urs Kleinholdermann was funded by the Clinician Scientist program (SUCCESS) of the Philipps University Marburg and the University Hospital of Marburg.

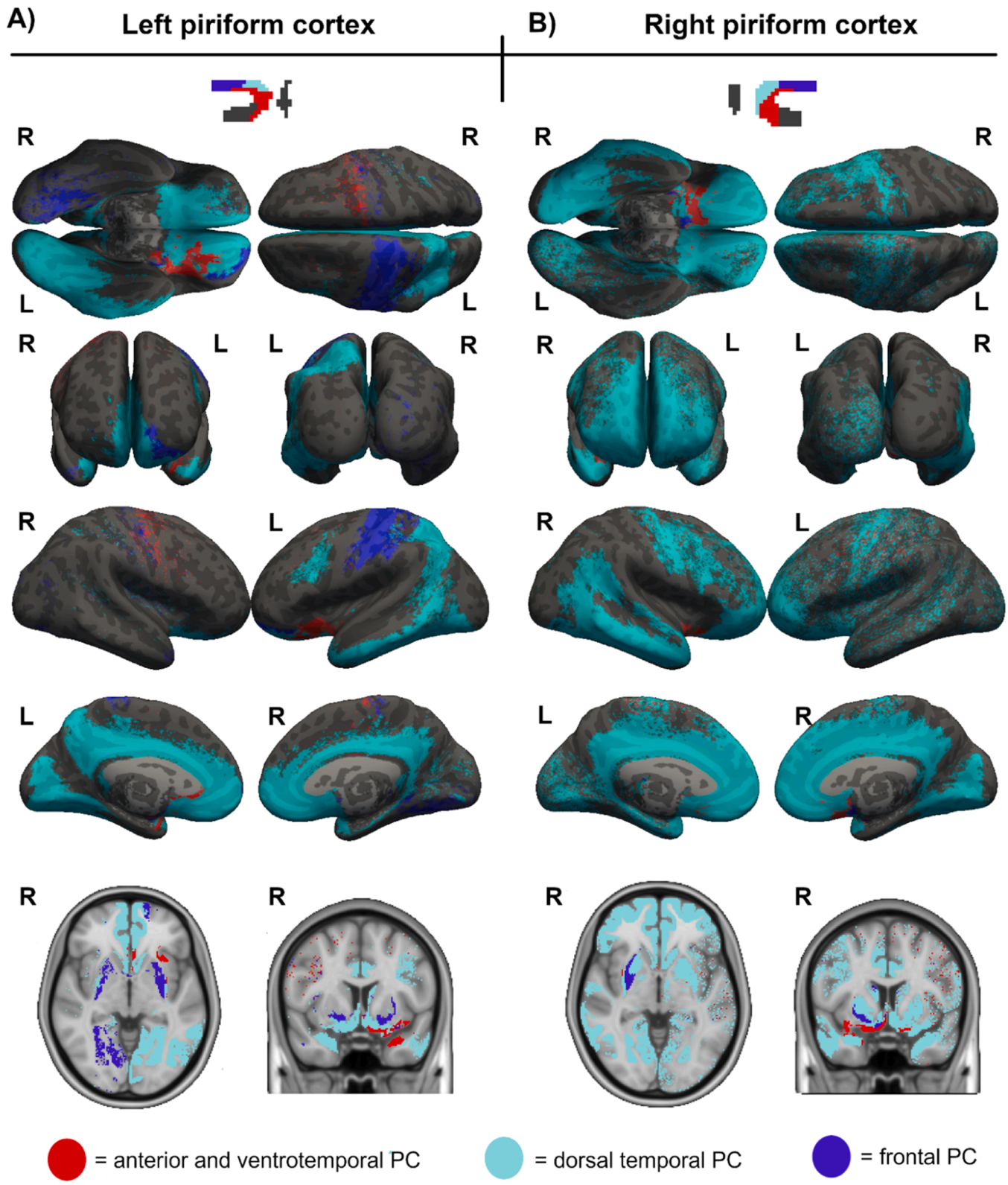

Fig. 11. Characterization of the cortex by its structural connectivity with each parcel from two exemplary clustering solutions (i.e., bilateral 7-cluster solutions). A) Connectivity of the left-sided parcellation, B) connectivity of the right-sided parcellation. Color indicates the cluster that exhibited the strongest connectivity among all clusters within a parcellation with a given gray matter voxel. Volume maps have been projected to the surface using freesurfer (cf. methods Section 2.7). Colors match those of clusters from Fig. 1. For clearer visualization, only connections of clusters within the PC are displayed. Background surface: inflated surface of the MNI152 brain. Background image, last row: MNI152 brain. *L*=left hemisphere, *R*=right hemisphere.

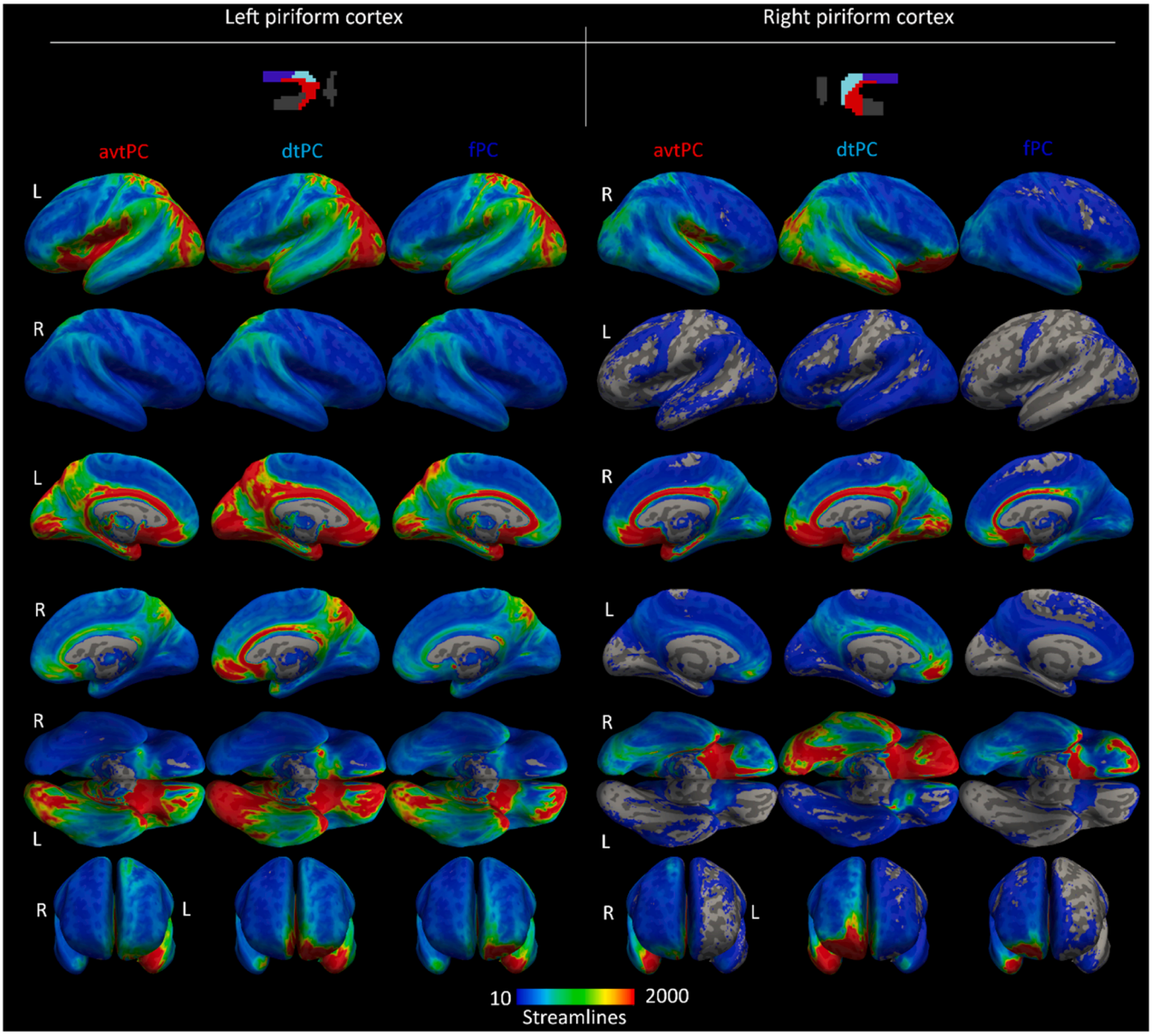

Fig. 12. Descriptive depiction of streamline counts shared between the cortical surface and bilateral PC subregions as obtained from bilateral 7-cluster solutions. Streamline counts were thresholded between 10 and 2000 streamlines for visualization. Background surface: inflated surface of the MNI152 brain. Background image, last row: MNI152 brain. *L*=left hemisphere, *R*=right hemisphere.

CRediT authorship contribution statement

F. Zahnert: Writing – review & editing, Writing – original draft, Visualization, Software, Methodology, Investigation, Formal analysis, Conceptualization. **U. Kleinholdermann:** Writing – review & editing, Writing – original draft, Visualization, Software, Methodology, Investigation, Formal analysis, Conceptualization. **M. Belke:** Writing – review & editing, Formal analysis. **B. Keil:** Writing – review & editing. **K. Menzler:** Writing – review & editing. **D.J. Pedrosa:** Writing – review & editing. **L. Timmermann:** Writing – review & editing. **T. Kircher:** Writing – review & editing. **I. Nenadić:** Writing – review & editing. **S. Knake:** Writing – review & editing, Supervision, Conceptualization.

Declaration of competing interest

FZ- None related to this work. Felix Zahnert has participated in a seminar on complex epilepsies funded by UCB**. UK**-None related to this work. Urs Kleinholdermann has participated in a DBS course industry funded by Boston Scientific Corp. **DJP**- None related to this work. David Pedrosa has received honoraria for speaking at symposia sponsored by Boston Scientific Corp, Medtronic, AbbVie Inc, Zambon and Esteve Pharmaceuticals GmbH. He has received honoraria as a consultant for Boston Scientific Corp and Bayer, and has received a grant from Boston Scientific Corp for a project entitled "Sensor-based optimisation of Deep Brain Stimulation settings in Parkinson's disease" (COMPARE-DBS). David Pedrosa's institution, not David Pedrosa himself, has received funding from the JNPD, the Horizon 2020 programme, the Parkinson's Foundation and, finally, David Pedrosa has been reimbursed for travel expenses to attend congresses by Esteve Pharmaceuticals GmbH and Boston Scientific Corp. **LT**- None related to this work. Between February 2018 and March 2023, Lars Timmermann received occasional payments as a consultant for Boston Scientific and also received honoraria as a speaker on symposia sponsored by UCB, Desitin, Boston Scientific, AbbVIE, Novartis, GlaxoSmithKline, Neuraxpharm, the Movement

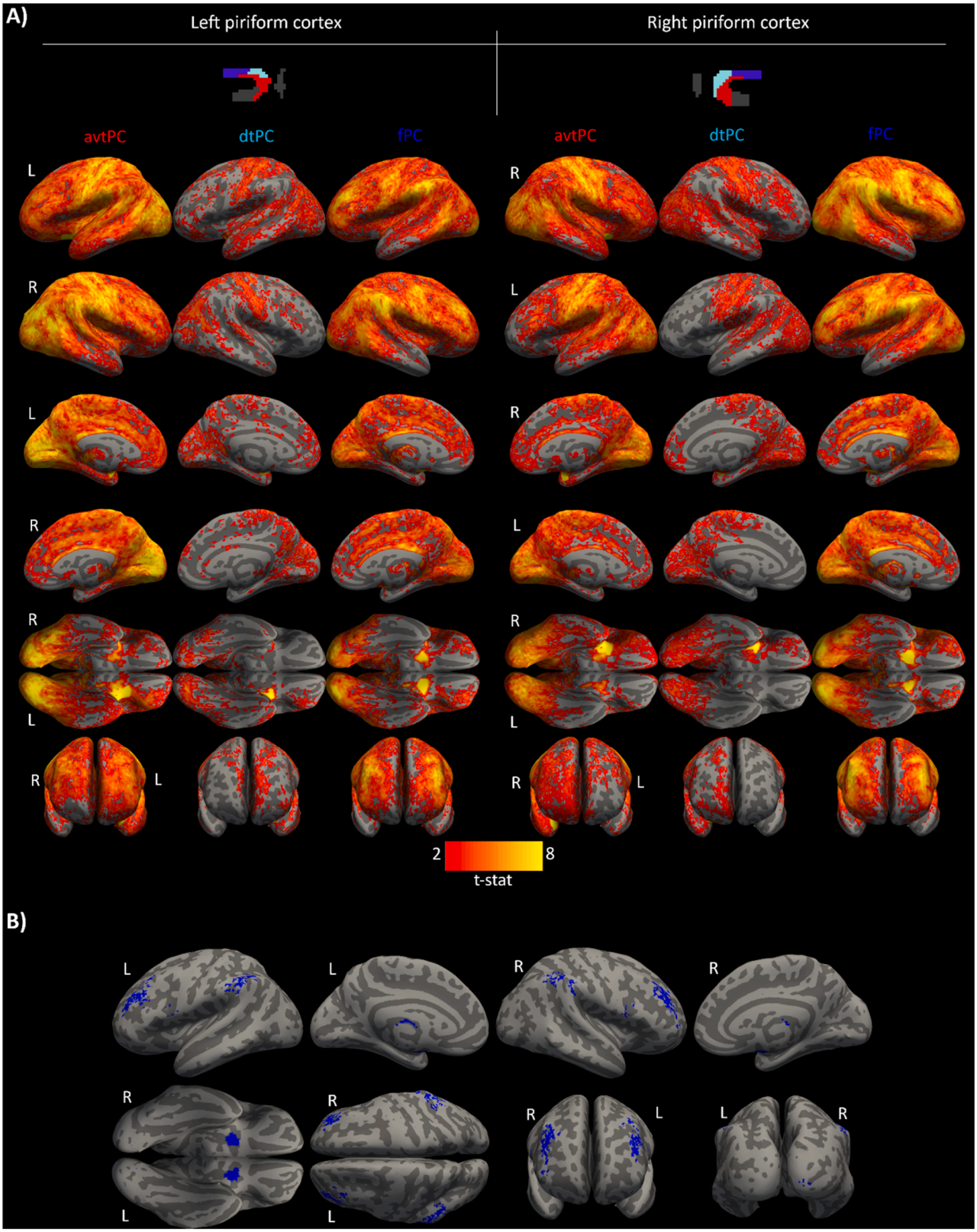

Fig. 13. **A)** T-maps of significant functional connectivity of piriform clusters that had been defined using diffusion MRI (bilateral 7-cluster solutions). T-maps were thresholded between values of $t = 2$–8 for better comparability. **B)** Summary of regions where bilateral f-PC (right and left tested separately) showed significantly stronger functional connectivity as compared to both respective ipsilateral dt-PC and f-PC clusters. Twelve paired permutation *t*-tests had been conducted to create contrasts between all clusters labeled as "PC" within each hemisphere (three each). In addition to the prior FWE-correction for multiple testing within FSL *randomise*, Bonferroni-correction for twelve tests was conducted, so that the corrected p-threshold for each image was set at 0.0042. Background surface: inflated surface of the MNI152 brain.

Disorders Society and DIAPLAN. The institution of Lars Timmermann, not Lars Timmermann personally received funding by Boston Scientific, the German Research Foundation, the German Ministry of Education and Research, the Otto-Loewi-Foundation and the Deutsche Parkinson Vereinigung. Neither Lars Timmermann nor any member of his family holds stocks, stock options, patents, or financial interests in any of the above-mentioned companies or their competitors. Lars Timmermann serves as the president of the German Neurological Society without any payment or any income. **SK**- None related to this work. Susanne Knake received consultant fees or speaker's honoraria from Arvelle, Bial, Epilog, Desitin, Precisis, UCB, and Zogenix.

The other authors declare no competing financial interests.

Data availability

Code and results are available at the project's github repository https://github.com/Zahnert/piriform_cbp. The human connectome project data used are freely available online.

Data and code availability

The code for the analyses conducted in this study is available at https://github.com/Zahnert/piriform_cbp. In addition, the seed ROI, target ROI and all parcellations and connectivity maps produced in this study can be found here. The Human Connectome Project data used in this study are freely available under https://www.humanconnectome.org/.

Acknowledgements

Data were provided by the Human Connectome Project, WU-Minn Consortium (Principal Investigators: David Van Essen and Kamil Ugurbil; 1U54MH091657) funded by the 16 NIH Institutes and Centers that support the NIH Blueprint for Neuroscience Research; and by the McDonnell Center for Systems Neuroscience at Washington University.

Supplementary materials

Supplementary material associated with this article can be found, in the online version, at doi:10.1016/j.neuroimage.2024.120747.

References

Abraham, A., Pedregosa, F., Eickenberg, M., Gervais, P., Mueller, A., Kossaifi, J., Gramfort, A., Thirion, B., Varoquaux, G., 2014. Machine learning for neuroimaging with scikit-learn. Front. Neuroinform. 8 https://doi.org/10.3389/fninf.2014.00014.

Allison, A.C., 1954. The secondary olfactory areas in the human brain. J. Anat. 88, 481–488.

Behrens, T.E.J., Berg, H.J., Jbabdi, S., Rushworth, M.F.S., Woolrich, M.W., 2007. Probabilistic diffusion tractography with multiple fibre orientations: what can we gain? Neuroimage 34, 144–155. https://doi.org/10.1016/j.neuroimage.2006.09.018.

Bensafi, M., Sobel, N., Khan, R.M., 2007. Hedonic-specific activity in piriform cortex during odor imagery mimics that during odor perception. J. Neurophysiol. 98, 3254–3262. https://doi.org/10.1152/jn.00349.2007.

Bitter, T., Gudziol, H., Burmeister, H.P., Mentzel, H.J., Guntinas-Lichius, O., Gaser, C., 2010. Anosmia2eas. Chem. Senses 35, 407–415. https://doi.org/10.1093/chemse/bjq028.

Borger, V., Hamed, M., Bahna, M., Rácz, Á., Ilic, I., Potthoff, A., Baumgartner, T., Rüber, T., Becker, A., Radbruch, A., Mormann, F., Surges, R., Vatter, H., Schneider, M., 2022. Temporal lobe epilepsy surgery: piriform cortex resection impacts seizure control in the long-term. Ann. Clin. Transl. Neurol. 9, 1206–1211. https://doi.org/10.1002/acn3.51620.

Borger, V., Schneider, M., Taube, J., Potthoff, A., Keil, V.C., Hamed, M., Aydin, G., Ilic, I., Solymosi, L., Elger, C.E., Güresir, E., Fimmers, R., Schuss, P., Helmstaedter, C., Surges, R., Vatter, H., 2021. Resection of piriform cortex predicts seizure freedom in temporal lobe epilepsy. Ann. Clin. Transl. Neurol. 8, 177–189. https://doi.org/10.1002/acn3.51263.

Brodman, K., 1909. Vergleichende Lokalisationslehre der Grosshirnrinde in Ihren Prinzipien dargestellt Auf Grund des Zellenbaues. JA Barth, Leipzig.

Carmichael, S.T., Clugnet, M.-C., Price, J.L., 1994. Central olfactory connections in the macaque monkey. J. Comp. Neurol. 346, 403–434. https://doi.org/10.1002/cne.903460306.

Cerf-Ducastel, B., Murphy, C., 2006. Neural substrates of cross-modal olfactory recognition memory: an fMRI study. Neuroimage 31, 386–396. https://doi.org/10.1016/j.neuroimage.2005.11.009.

Courtiol, E., Buonviso, N., Litaudon, P., 2019. Odorant features differentially modulate beta/gamma oscillatory patterns in anterior versus posterior piriform cortex. Neuroscience 409, 26–34. https://doi.org/10.1016/j.neuroscience.2019.04.025.

Crosby, E.C., Humphrey, T., 1941. Studies of the vertebrate telencephalon. II. The nuclear pattern of the anterior olfactory nucleus, tuberculum olfactorium and the amygdaloid complex in adult man. J. Comp. Neurol. 74, 309–352. https://doi.org/10.1002/cne.900740209.

Dale, A.M., Fischl, B., Sereno, M.I., 1999. Cortical surface-based analysis. Neuroimage 9, 179–194. https://doi.org/10.1006/nimg.1998.0395.

Echevarria-Cooper, S.L., Zhou, G., Zelano, C., Pestilli, F., Parrish, T.B., Kahnt, T., 2022. Mapping the microstructure and striae of the human olfactory tract with diffusion MRI. J. Neurosci. 42, 58–68. https://doi.org/10.1523/JNEUROSCI.1552-21.2021.

Eickhoff, S.B., Thirion, B., Varoquaux, G., Bzdok, D., 2015. Connectivity-based parcellation: critique and implications. Hum. Brain Mapp. 36, 4771–4792. https://doi.org/10.1002/hbm.22933.

Fischl, B., Salat, D.H., Busa, E., Albert, M., Dieterich, M., Haselgrove, C., van der Kouwe, A., Killiany, R., Kennedy, D., Klaveness, S., Montillo, A., Makris, N., Rosen, B., Dale, A.M., 2002. Whole brain segmentation: automated labeling of neuroanatomical structures in the human brain. Neuron 33, 341–355. https://doi.org/10.1016/s0896-6273(02)00569-x.

Fischl, B., Sereno, M.I., Dale, A.M., 1999. Cortical surface-based analysis. Neuroimage 9, 195–207. https://doi.org/10.1006/nimg.1998.0396.

Galovic, M., Baudracco, I., Wright-Goff, E., Pillajo, G., Nachev, P., Wandschneider, B., Woermann, F., Thompson, P., Baxendale, S., McEvoy, A.W., Nowell, M., Mancini, M., Vos, S.B., Winston, G.P., Sparks, R., Prados, F., Miserocchi, A., de Tisi, J., Van Graan, L.A., Rodionov, R., Wu, C., Alizadeh, M., Kozlowski, L., Sharan, A.D., Kini, L. G., Davis, K.A., Litt, B., Ourselin, S., Moshé, S.L., Sander, J.W.A., Löscher, W., Duncan, J.S., Koepp, M.J., 2019. Association of piriform cortex resection with surgical outcomes in patients with temporal lobe epilepsy. JAMa Neurol. 76, 690. https://doi.org/10.1001/jamaneurol.2019.0204.

Ghosh, S., Larson, S.D., Hefzi, H., Marnoy, Z., Cutforth, T., Dokka, K., Baldwin, K.K., 2011. Sensory maps in the olfactory cortex defined by long-range viral tracing of single neurons. Nature 472, 217–220. https://doi.org/10.1038/nature09945.

Glasser, M.F., Coalson, T.S., Robinson, E.C., Hacker, C.D., Harwell, J., Yacoub, E., Ugurbil, K., Andersson, J., Beckmann, C.F., Jenkinson, M., Smith, S.M., van Essen, D. C., 2016. A multi-modal parcellation of human cerebral cortex. Nature 536, 171–178. https://doi.org/10.1038/nature18933.

Glasser, M.F., Sotiropoulos, S.N., Wilson, J.A., Coalson, T.S., Fischl, B., Andersson, J.L., Xu, J., Jbabdi, S., Webster, M., Polimeni, J.R., Van Essen, D.C., Jenkinson, M., 2013. The minimal preprocessing pipelines for the human connectome project. Neuroimage 80, 105–124. https://doi.org/10.1016/j.neuroimage.2013.04.127.

Gonçalves Pereira, P.M., Insausti, R., Artacho-Pérula, E., Salmenperä, T., Kälviäinen, R., Pitkänen, A, 2005. MR volumetric analysis of the piriform cortex and cortical amygdala in drug-refractory temporal lobe epilepsy. AJNR Am. J. Neuroradiol. 26, 319–332.

Gottfried, J.A., Deichmann, R., Winston, J.S., Dolan, R.J., 2002. Functional heterogeneity in human olfactory cortex: an event-related functional magnetic resonance imaging study. J. Neurosci. 22, 10819–10828. https://doi.org/10.1523/JNEUROSCI.22-24-10819.2002.

Gottfried, J.A., Dolan, R.J., 2003. The nose smells what the eye sees. Neuron 39, 375–386. https://doi.org/10.1016/S0896-6273(03)00392-1.

Haberly, L.B., 2001. Parallel-distributed processing in olfactory cortex: new insights from morphological and physiological analysis of neuronal circuitry. Chem. Senses 26, 551–576. https://doi.org/10.1093/chemse/26.5.551.

Haberly, L.B., 2022. Recruitment of interictal- and ictal-like discharges in posterior piriform cortex by delta-rate (1-4 Hz) focal bursts in anterior piriform cortex in vivo. Epilepsy Res. 187, 107032 https://doi.org/10.1016/j.eplepsyres.2022.107032.

Howard, J.D., Plailly, J., Grueschow, M., Haynes, J.-D., Gottfried, J.A., 2009. Odor quality coding and categorization in human posterior piriform cortex. Nat. Neurosci. 12, 932–938. https://doi.org/10.1038/nn.2324.

ImageMagick Studio LLC. 2017. ImageMagick.

Jbabdi, S., Sotiropoulos, S.N., Savio, A.M., Graña, M., Behrens, T.E.J., 2012. Model-based analysis of multishell diffusion MR data for tractography: how to get over fitting problems. Magn. Reson. Med. 68, 1846–1855. https://doi.org/10.1002/mrm.24204.

Johnson, D.M.G., Illig, K.R., Behan, M., Haberly, L.B., 2000. New features of connectivity in piriform cortex visualized by intracellular injection of pyramidal cells suggest that "Primary" olfactory cortex functions like "Association" cortex in other sensory systems. J. Neurosci. 20, 6974–6982. https://doi.org/10.1523/JNEUROSCI.20-18-06974.2000.

Kajiwara, R., Tominaga, T., Takashima, I., 2007. Olfactory information converges in the amygdaloid cortex via the piriform and entorhinal cortices: observations in the guinea pig isolated whole-brain preparation. Eur. J. Neurosci. 25, 3648–3658. https://doi.org/10.1111/j.1460-9568.2007.05610.x.

Krettek, J.E., Price, J.L., 1977. Projections from the amygdaloid complex and adjacent olfactory structures to the entorhinal cortex and to the subiculum in the rat and cat. J. Comp. Neurol. 172, 723–752. https://doi.org/10.1002/cne.901720409.

Lane, G., Zhou, G., Noto, T., Zelano, C., 2020. Assessment of direct knowledge of the human olfactory system. Exp. Neurol. 329, 113304 https://doi.org/10.1016/j.expneurol.2020.113304.

Litaudon, P., Amat, C., Bertrand, B., Vigouroux, M., Buonviso, N., 2003. Piriform cortex functional heterogeneity revealed by cellular responses to odours. Eur. J. Neurosci. 17, 2457–2461. https://doi.org/10.1046/j.1460-9568.2003.02654.x.

Löscher, W., Lehmann, H., Ebert, U., 1998. Differences in the distribution of GABA- and GAD-immunoreactive neurons in the anterior and posterior piriform cortex of rats. Brain Res. 800, 21–31. https://doi.org/10.1016/s0006-8993(98)00488-0.

Mai, J.K., Majtanik, M., Paxinos, G., 2015. Atlas of the Human Brain, 4th edition. Academic Press, an imprint of Elsevier, Amsterdam.

Miyamichi, K., Amat, F., Moussavi, F., Wang, C., Wickersham, I., Wall, N.R., Taniguchi, H., Tasic, B., Huang, Z.J., He, Z., Callaway, E.M., Horowitz, M.A., Luo, L., 2011. Cortical representations of olfactory input by trans-synaptic tracing. Nature 472, 191–196. https://doi.org/10.1038/nature09714.

Pedregosa F., Varoquaux G., Gramfort A., Michel V., Thirion B., Grisel O., Blondel M., Müller A., Nothman J., Louppe G., Prettenhofer P., Weiss R., Dubourg V., Vanderplas J., Passos A., Cournapeau D., Brucher M., Perrot M., Duchesnay É. 2018. Scikit-learn: machine Learning in Python.

Porter, J., Anand, T., Johnson, B., Khan, R.M., Sobel, N., 2005. Brain mechanisms for extracting spatial information from smell. Neuron 47, 581–592. https://doi.org/10.1016/j.neuron.2005.06.028.

Reuter, N., Genon, S., Kharabian Masouleh, S., Hoffstaedter, F., Liu, X., Kalenscher, T., Eickhoff, S.B., Patil, K.R, 2020. CBPtools: a Python package for regional connectivity-based parcellation. Brain Struct. Funct. 225, 1261–1275. https://doi.org/10.1007/s00429-020-02046-1.

Salimi-Khorshidi, G., Douaud, G., Beckmann, C.F., Glasser, M.F., Griffanti, L., Smith, S. M., 2014. Automatic denoising of functional MRI data: combining independent component analysis and hierarchical fusion of classifiers. Neuroimage 90, 449–468. https://doi.org/10.1016/j.neuroimage.2013.11.046.

Schulze, P., Bestgen, A.-K., Lech, R.K., Kuchinke, L., Suchan, B., 2017. Preprocessing of emotional visual information in the human piriform cortex. Sci. Rep. 7, 9191. https://doi.org/10.1038/s41598-017-09295-x.

Smith, S.M., Beckmann, C.F., Andersson, J., Auerbach, E.J., Bijsterbosch, J., Douaud, G., Duff, E., Feinberg, D.A., Griffanti, L., Harms, M.P., Kelly, M., Laumann, T., Miller, K. L., Moeller, S., Petersen, S., Power, J., Salimi-Khorshidi, G., Snyder, A.Z., Vu, A.T., Woolrich, M.W., Xu, J., Yacoub, E., Uğurbil, K., Van Essen, D.C., Glasser, M.F, 2013. Resting-state fMRI in the human connectome project. Neuroimage 80, 144–168. https://doi.org/10.1016/j.neuroimage.2013.05.039.

Sotiropoulos, S.N., Moeller, S., Jbabdi, S., Xu, J., Andersson, J.L., Auerbach, E.J., Yacoub, E., Feinberg, D., Setsompop, K., Wald, L.L., Behrens, T.E.J., Ugurbil, K., Lenglet, C., 2013. Effects of image reconstruction on fiber orientation mapping from multichannel diffusion MRI: reducing the noise floor using SENSE: effects of dMRI Image Reconstruction on Fiber Orientations. Magn. Reson. Med. 70, 1682–1689. https://doi.org/10.1002/mrm.24623.

Sotiropoulos, S.N., Zalesky, A., 2019. Building connectomes using diffusion MRI: why, how and but. NMR Biomed 32, e3752. https://doi.org/10.1002/nbm.3752.

Steinbart, D., Yaakub, S.N., Steinbrenner, M., Guldin, L.S., Holtkamp, M., Keller, S.S., Weber, B., Rüber, T., Heckemann, R.A., Ilyas-Feldmann, M., Hammers, A., 2023. Automatic and manual segmentation of the piriform cortex: method development and validation in patients with temporal lobe epilepsy and Alzheimer's disease. Hum. Brain Mapp. 44, 3196–3209. https://doi.org/10.1002/hbm.26274.

Steinley, D., 2004. Properties of the Hubert-Arabie adjusted Rand index. Psychol. Methods 9, 386–396. https://doi.org/10.1037/1082-989X.9.3.386.

Uğurbil, K., Xu, J., Auerbach, E.J., Moeller, S., Vu, A.T., Duarte-Carvajalino, J.M., Lenglet, C., Wu, X., Schmitter, S., Van de Moortele, P.F., Strupp, J., Sapiro, G., De Martino, F., Wang, D., Harel, N., Garwood, M., Chen, L., Feinberg, D.A., Smith, S.M., Miller, K.L., Sotiropoulos, S.N., Jbabdi, S., Andersson, J.L.R., Behrens, T.E.J., Glasser, M.F., Van Essen, D.C., Yacoub, E., 2013. Pushing spatial and temporal resolution for functional and diffusion MRI in the human connectome project. Neuroimage 80, 80–104. https://doi.org/10.1016/j.neuroimage.2013.05.012.

Van Essen, D.C., Ugurbil, K., Auerbach, E., Barch, D., Behrens, T.E.J., Bucholz, R., Chang, A., Chen, L., Corbetta, M., Curtiss, S.W., Della Penna, S., Feinberg, D., Glasser, M.F., Harel, N., Heath, A.C., Larson-Prior, L., Marcus, D., Michalareas, G., Moeller, S., Oostenveld, R., Petersen, S.E., Prior, F., Schlaggar, B.L., Smith, S.M., Snyder, A.Z., Xu, J., Yacoub, E, 2012. The Human Connectome Project: a data acquisition perspective. Neuroimage 62, 2222–2231. https://doi.org/10.1016/j.neuroimage.2012.02.018.

Vaughan, D.N., Jackson, G.D., 2014. The piriform cortex and human focal epilepsy. Front. Neurol. 5 https://doi.org/10.3389/fneur.2014.00259.

von Economo, C., Koskinas, G., 1925. Die Cytoarchitektonik der Hirnrinde des erwachsenen Menschen. Textband Und Atlas. Springer, Wien.

Yang, Y., Wang, X., 2020. Odor modulates hand movements in a Reach-to-Grasp task. Front. Neurosci. 14, 560. https://doi.org/10.3389/fnins.2020.00560.

Zelano, C., Bensafi, M., Porter, J., Mainland, J., Johnson, B., Bremner, E., Telles, C., Khan, R., Sobel, N., 2005. Attentional modulation in human primary olfactory cortex. Nat. Neurosci. 8, 114–120. https://doi.org/10.1038/nn1368.

Zelano, C., Mohanty, A., Gottfried, J.A., 2011. Olfactory predictive codes and stimulus templates in piriform cortex. NeuronNeuron 72, 178–187. https://doi.org/10.1016/j.neuron.2011.08.010.

Zelano, C., Sobel, N., 2005. Humans as an animal model for systems-level organization of olfaction. Neuron 48, 431–454. https://doi.org/10.1016/j.neuron.2005.10.009.

Zhou, G., Lane, G., Cooper, S.L., Kahnt, T., Zelano, C., 2019. Characterizing functional pathways of the human olfactory system. Elife 8, e47177. https://doi.org/10.7554/eLife.47177.

Zhou, G., Olofsson, J.K., Koubeissi, M.Z., Menelaou, G., Rosenow, J., Schuele, S.U., Xu, P., Voss, J.L., Lane, G., Zelano, C., 2021. Human hippocampal connectivity is stronger in olfaction than other sensory systems. Prog. Neurobiol. 201, 102027 https://doi.org/10.1016/j.pneurobio.2021.102027.